

Oxygen Transport Ceramic Membranes

Quarterly Report

April-June 2001

By:

Dr. Sukumar Bandopadhyay
and
Dr. Nagendra Nagabhushana

School of Mineral Engineering
University of Alaska Fairbanks

Issued: July 2001

DOE Award # DE-FC26-99FT400054

University of Alaska Fairbanks
School of Mineral Engineering
Brooks 209
Fairbanks, AK 99775

DISCLAIMER

This report was prepared as an account of work sponsored by an agency of the United States Government. Neither the United States Government nor any agency thereof, nor any of their employees, makes any warrantee, express or implied, or assumes any legal liability or responsibility for the accuracy, completeness, or usefulness of any information, apparatus, product, or process disclosed, or represents that its use would not infringe privately owned rights. Reference herein to any specific commercial product, process, or service by trade name, trademark, manufacturer, or otherwise does not necessarily constitute or imply its endorsement, recommendation, or favoring by the United States Government or any agency thereof. The views and opinions of the authors expressed herein do not necessarily state or reflect those of the United States Government or any agency thereof.

Executive Summary

Conversion of natural gas to liquid fuels and chemicals is a major goal for the Nation as it enters the 21st Century. Technically robust and economically viable processes are needed to capture the value of the vast reserves of natural gas on Alaska's North Slope, and wean the Nation from dependence on foreign petroleum sources. Technologies that are emerging to fulfill this need are all based syngas as an intermediate. Syngas (a mixture of hydrogen and carbon monoxide) is a fundamental building block from which chemicals and fuels can be derived. Lower cost syngas translates directly into more cost-competitive fuels and chemicals.

The currently practiced commercial technology for making syngas is either steam methane reforming (SMR) or a two-step process involving cryogenic oxygen separation followed by natural gas partial oxidation (POX). These high-energy, capital-intensive processes do not always produce syngas at a cost that makes its derivatives competitive with current petroleum-based fuels and chemicals.

In the mid 80's BP invented a radically new technology concept that will have a major economic and energy efficiency impact on the conversion of natural gas to liquid fuels, hydrogen, and chemicals.¹ This technology, called Electropox, integrates oxygen separation with the oxidation and steam reforming of natural gas into a single process to produce syngas with an economic advantage of 30 to 50 percent over conventional technologies.²

The Electropox process uses novel and proprietary solid metal oxide ceramic oxygen transport membranes [OTMs], which selectively conduct both oxide ions and electrons through their lattice structure at elevated temperatures.³ Under the influence of an oxygen

¹Mazanec, T. J.; Cable, T. L.; Frye, J. G., Jr.; US 4,793,904, 27 Dec **1988**, assigned to The Standard Oil Company (now BP America), Mazanec, T. J.; Cable, T. L.; US 4,802,958, 7 Feb **1989**, assigned to the Standard Oil Co. (now BP America), Cable, T. L.; Mazanec, T. J.; Frye, J. G., Jr.; European Patent Application 0399833, 24 May **1990**, published 28 November **1990**.

²Bredesen, R.; Sogge, J.; "A Technical and Economic Assessment of Membrane Reactors for Hydrogen and Syngas Production" presented at Seminar on the Ecol. Applic. of Innovative Membrane Technology in the Chemical Industry", Cetraro, Calabria, Italy, 1-4 May **1996**.

³Mazanec, T.J., *Interface*, **1996**; Mazanec, T.J., *Solid State Ionics*, 70/71, **1994** 11-19; "Electropox: BP's Novel Oxidation Technology", T.J. Mazanec, pp 212-225, in "The Role of Oxygen in Improving Chemical Processes", M. Fetizon and W.J. Thomas, eds, Royal Society of Chemistry, London, **1993**; "Electropox:

partial pressure gradient, oxygen ions move through the dense, nonporous membrane lattice at high rates with 100 percent selectivity. Transported oxygen reacts with natural gas on the fuel side of the ceramic membrane in the presence of a catalyst to produce syngas.

In 1997 BP entered into an OTM Alliance with Praxair, Amoco, Statoil and Sasol to advance the Electropox technology in an industrially sponsored development program. These five companies have been joined by Phillips Petroleum and now are carrying out a multi-year \$40+ million program to develop and commercialize the technology. The program targets materials, manufacturing and engineering development issues and culminates in the operation of semi-works and demonstration scale prototype units.

The Electropox process represents a truly revolutionary technology for conversion of natural gas to synthesis gas not only because it combines the three separate unit operations of oxygen separation, methane oxidation and methane steam reforming into a single step, but also because it employs a chemically active ceramic material in a fundamentally new way. On numerous fronts the commercialization of Electropox demands solutions to problems that have never before been accomplished. Basic problems in materials and catalysts, membrane fabrication, model development, and reactor engineering all need solutions to achieve commercial success.

Six important issues have been selected as needing understanding on a fundamental level at which the applied Alliance program cannot achieve the breadth and depth of understanding needed for rapid advancement. These issues include

1. Oxygen diffusion kinetics (University of Houston)
2. Grain structure and atomic segregation (University of Illinois - Chicago)
3. Phase stability and stress development (University of Missouri - Rolla)
4. Mechanical property evaluation in thermal and chemical stress fields (University of Alaska Fairbanks)
5. Graded ceramic/metal seals (Massachusetts Institute of Technology)

BP's Novel Oxidation Technology", T.J. Mazanec, pp 85-96, in "The Activation of Dioxygen and Homogeneous Catalytic Oxidation", D.H.R. Barton, A. E. Martell, D.T. Sawyer, eds, Plenum Press, New York, **1993**; "Electrocatalytic Cells for Chemical Reaction", T.J. Mazanec, T.L. Cable, J.G. Frye, Jr.; Prep Petrol Div ACS, San Fran, **1992** 37, 135-146; T.J. Mazanec, T.L. Cable, J.G. Frye, Jr.; *Solid State Ionics*, **1992**, 53-56, 111-118.

Statement of Work

- Task 1 Design, fabricate and evaluate ceramic to metal seals based on graded ceramic powder / metal braze joints.
- Task 2 Evaluate the effect of defect configuration on ceramic membrane conductivity and long term chemical and structural stability.
- Task 3 Determine materials mechanical properties under conditions of high temperatures and reactive atmospheres.
- Task 4 Evaluate phase stability and thermal expansion of candidate perovskite membranes and develop techniques to support these materials on porous metal structures.
- Task 5 Assess the microstructure of membrane materials to evaluate the effects of vacancy-impurity association, defect clusters, and vacancy-dopant association on the membrane performance and stability.
- Task 6 Measure kinetics of oxygen uptake and transport in ceramic membrane materials under commercially relevant conditions using isotope labeling techniques.

Task 1 & 2

Development of Ceramic Membrane/Metal Joints

**Prof. Thomas W. Eagar, Dr Harold R Larson,
Mr Raymundo Arroyave and Ms Jocelyn L. Wiese**

ABSTRACT

The mechanical properties of model systems were analyzed. A reasonably accurate finite element model was implemented and a rational metric to predict the strength of ceramic/metal concentric joints was developed. The mode of failure of the ceramic/metal joints was determined and the importance of the mechanical properties of the braze material was assessed. Thermal cycling experiments were performed on the model systems and the results were discussed. Additionally, experiments using the concept of placing diffusion barriers on the ceramic surface to limit the extent of the reaction with the braze were performed. It was also observed that the nature and morphology of the reaction zone depends greatly on the nature of the perovskite structure being used. From the experiments, it is observed that the presence of Cr in the Fe-occupied sites decreases the tendency of Fe to segregate and to precipitate out of the lattice. In these new experiments, Ni was observed to play a major role in the decomposition of the ceramic substrate.

Mechanical Properties of the Joints

Testing techniques are being developed to measure and understand the mechanical properties of concentric metal-to-ceramic joints. A model system of alumina tubes brazed around nickel- and iron-based alloys using Ticusil™ (Ag-Cu-Ti) brazing alloy has been used as a model system. The testing and analytical methods that have been developed will be applied to the “perovskite/Haynes 230® system once brazing alloys have been developed for those materials and mechanical property data for the ceramic is available.

Use of the Finite Element Model as a Tool to Predict Joint Shear Strength

A finite element model was built using ABAQUS to simulate the residual stresses that develop in the joint during cooling from 780C to room temperature. The residual stresses, as well as elastic and plastic strain energy present in each joint component (ceramic, base metal, filler metal) were calculated

in the model. Models were developed for the four base metal – alumina combinations, and in the same geometries as the experimental shear-tested samples.

The relationship between joint length and each component of strain energy in the filler metal was calculated from the data generated by the models, for each type of joint. The theoretical amount of strain energy present in each shear-tested joint was calculated from these relationships.

Since it is the residual stresses in a metal-to-ceramic brazed joint that degrade the strength of the joint, there ought to exist a correlation between strain energy and joint shear strength. Furthermore, since residual stresses are a function of joint geometry and materials, this correlation should hold for joints made with different substrates. The strain energy – joint strength data for all samples were plotted together, and R^2 values calculated (Figure 1). Both the plastic strain energy and total strain energy present in the filler metal correlate quite well with joint strength.

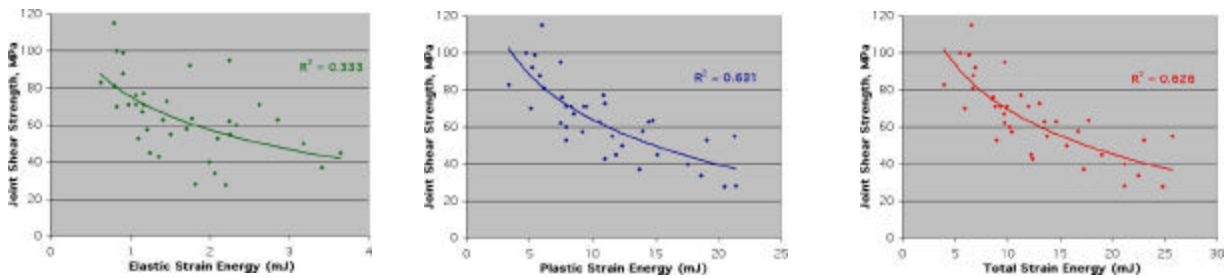


Figure 1: Correlations between measured joint shear strength and calculated elastic, plastic, and total strain energy in the filler metal.

The correlation between joint strength and strain energy reported in the previous report and depicted in the figure above means that it is in principle possible to predict joint strength of ceramic/metal seals once the mechanical properties of the components of the joints are known.

From the work on the mechanical strength of ceramic/metal interfaces, important conclusions can be drawn that have applicability for the particular problem of perovskite/metal seals:

- The plastic deformation of the interlayer plays a significant role in determining the mechanical strength of a ceramic/metal interface. For the particular case of perovskite/metal seals, it could be inferred that by properly selecting the interlayer material, the strength of the seal can be maximized.
- The total strain energy of the ceramic/metal system appears to be a good indicator for the comparison of the influence of different base metals of the final mechanical strength of ceramic/metal systems.
- The coefficient of thermal expansion between the base metal and ceramic is the most important physical property influencing the strain energy in the filler metal and the theoretical strength of the joints. The yield stress of the base metal is of secondary importance.
- The morphology of the filler metal in joints varied with the base metal. Nickel from the base metal tended to dissolve into the filler metal, altering the microstructure. This is particularly important when applied to the perovskite/metal systems. As has been seen in previous reports, the rate of the reaction between nickel-based alloys and perovskite substrates is such that vast reaction zones develop at the ceramic/metal interface. The chemical nature and morphology of these zones has been observed to play an important role in the nucleation of cracks that eventually lead to joint failure.

Perovskite/Metal Interactions

For the period reported in the present document, investigation of the reaction between nickel-based brazing alloys and perovskite/substrates has been continued. As has been said in previous reports, the goal of reactive brazing of ceramic/metal joints is the formation of a reaction product at the ceramic/metal interface such that the interfacial energy is reduced and the work of adhesion is increased. This increase in the work of adhesion increases in turn the maximum load that the joint can support before fracture. Usually the ceramic substrate is so thermochemically stable that no ceramic/metal reaction is likely to occur and therefore wetting is prevented and no stable interface is created.

For the particular situation of perovskite/metal interactions, it was found that the problem lied at the other extreme of the spectrum: the reaction of the ceramic substrate with the nickel-based braze alloy

used was so intense and extensive that the ceramic closest underwent local reduction and decomposition. This decomposition zone has been observed to be the origin of cracks that debilitate the strength of the ceramic/metal seal created. Under thermal cycling conditions, these initially small cracks would be expected to grow until fracture conditions (due to thermal stresses at the joint) would ensue.

As it became evident that the extent of the reaction needed to be limited somehow, the focus of the experimental program was switched to the creation of diffusion barriers on top of the ceramic substrate. These diffusion barriers would be able to still promote adhesion to the perovskite surface but at the same time would limit the extent of the reaction with the braze.

A series of experiments was devised to determine the potential use of diffusion barriers to limit the extent of the reaction at the ceramic/metal interface. Because of external factors, the ceramic used in this occasion was different from the first series of experiments, so no direct comparison between previous and new results was possible. For the diffusion-barrier experiments, the ceramic used was $\text{La}_{0.2}\text{Sr}_{0.8}\text{Cr}_{0.2}\text{Fe}_{0.8}\text{O}_3$. A nickel-based super alloy was used as the metal substrate and the same Ni-B brazing alloy was used as the bonding interlayer.

The samples were cut in 0.5" Dia x 0.1" thick disks, and then polished to 600 GRIT. After that, the samples were ultrasonically cleaned in isopropyl alcohol. The ceramic disks were conditioned in a N_2 atmosphere at 500 C for 2 hours before the experiments. For the actual joining experiments, the same high-temperature vacuum furnace was used. Temperature ramping up and down was controlled to minimize the possibilities of joint failure due to thermal shock. To keep the joint in place while joining, a slight pressure was applied.

Below we present the previous results concerning the experiments described above:

Perovskite / Cr / Ni-B / Inconel:

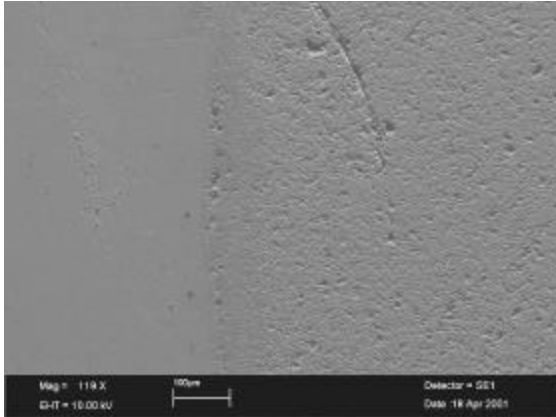


Figure 2 Perovskite/Cr/Ni-B/Inconel Joint. SEM , secondary electron image.

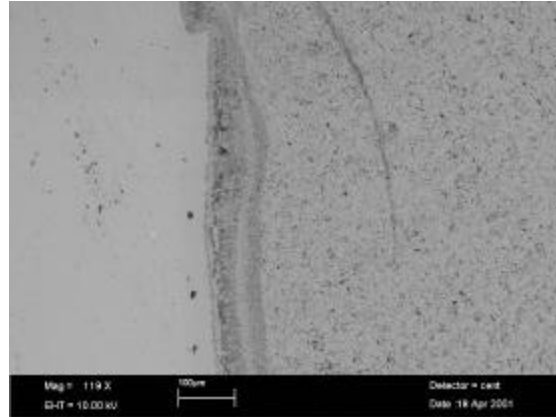


Figure 3 Perovskite/Cr/Ni-B/Inconel Joint. SEM , backscattered image.

From the figures above, it can be observed that an interface was formed between the braze metal and the perovskite surface. Contrary to our expectations, though, the Cr layer sputtered on the ceramic surface was somehow dissolved by the braze and the reaction with the ceramic was rather extensive (the reaction zone was almost as wide as in the previous series of experiments). It was also observed that the nature of the interactions between the ceramic and the braze were different from those observed with the $\text{La}_{0.6}\text{Sr}_{0.4}\text{FeO}_3$ perovskite:

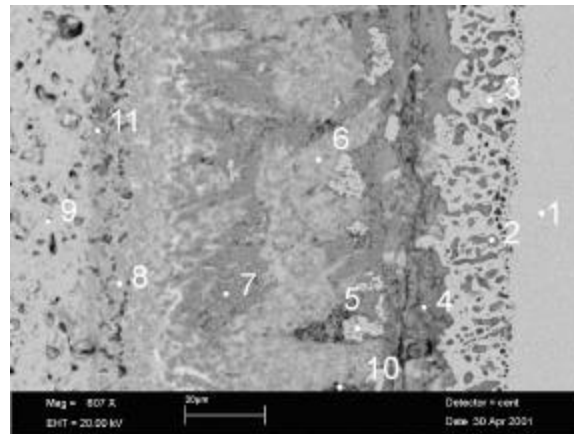


Figure 4 Perovskite/Cr/Ni-B/Inconel Joint. SEM , backscattered image. 807X

	1	2	3	4	5	6	7	8	9	10	11
Ni	81.6	96.5	25.5	4.7	4.0	17.3	4.0	1.1		4.1	1.5
Cr	8.2	1.3	11.6	9.8	3.4	2.9	2.4	0.8	3.1	3.0	3.2
Fe	4.6	2.1	6.0	12.4	9.2	8.2	9.5	4.8	12.6	9.0	12.3
Sr				13.8	9.4	6.5	10.7	15.6	16.3	9.7	11.4
La					0.1	2.6	1.4	5.7	4.2	3.5	3.0
O			56.9	59.4	73.9	62.4	72.0	72.1	63.8	70.7	68.6
Si	5.4										

Another important difference between the reactions observed in the previous experiments with $\text{La}_{0.6}\text{Sr}_{0.4}\text{FeO}_3$ perovskites and those observed in these $\text{La}_{0.2}\text{Sr}_{0.8}\text{Cr}_{0.2}\text{Fe}_{0.8}\text{O}_3$ /Metal joints was the absence of a La-O layer in direct contact with the braze. When La is the mayor component in the A sites of the perovskite structure, the formation of La-O compounds appears very likely. When this is not the case, however, La appears to segregate towards the perovskite (see figure and table above). Another important difference is the formation of a complex Ni-Cr-O (point 3) layer in direct contact with the braze. This implies that local reduction of the perovskite surface is taking place. The local oxygen chemical potential at the interface must thus be such that decomposition of the perovskite structure is favorable ($p\text{O}_2$ around 10^{-16}). A very interesting feature of this layer is the presence of highly metallic precipitates with Ni (point 2) as their major component (96%). As we go deeper into the reaction zone, Sr appears as a major component of the reaction products. La, on the other hand, does not appear at all in this region (point 4). It has been observed that this region is most likely to be the nucleation site of cracks that run parallel to the ceramic/metal interface and further characterization of the reaction products in this area appears to be necessary.

At approximately 30 microns from the ceramic/metal interface, no noticeable changes in composition can be observed. In fact, it is not unreasonable to infer that the only difference between this region and the bulk perovskite ceramic is the presence of brazing alloy inside the pores of the material:

When comparing the results of both series of experiments, it results evident that Ni appears to be playing a major role in the these $\text{La}_{0.2}\text{Sr}_{0.8}\text{Cr}_{0.2}\text{Fe}_{0.8}\text{O}_3$ /Metal experiments, which is not the case in the La-Sr-Fe-O/Metal reactions. Ni has been observed to be present at a depth of 60 microns into the reaction zone. This could be explained by the fact that the La-Sr-Cr-Fe-O perovskite samples presented an extremely high porosity. The braze, therefore, would be able to infiltrate the ceramic up to a large extent. The porosity is thus “healed” by the presence of this liquid metal. The problem with this,

though, is that the difference in expansion coefficients between the porous matrix and the filling medium can lead to a weakening of the matrix, as cooling and heating cycles proceed.

Perovskite / TiO / Ni-B / Inconel:

In the previous experiments it was observed that Cr-based diffusion barriers were not able to stop the extensive reaction occurring at the perovskite/braze interface. In fact, it was inferred from the experimental results that the nickel-based brazing alloy effectively dissolved the Cr deposited on top of the ceramic surface.

In previous experiments, Ti-sputtered layers were deposited on top of zirconia-based ceramic substrates. The aim of those experiments was to explore the possibility of using these reactive layers in conjunction with a non-reactive brazing alloy (Ni-based). It was observed then that the Ti-sputtered layer reacted with the zirconia substrate to form a titanium oxide (presumably TiO). The Ni-based brazing alloy would in turn wet the oxide and a ceramic/metal interface would be created, as can be seen in Figure 5.

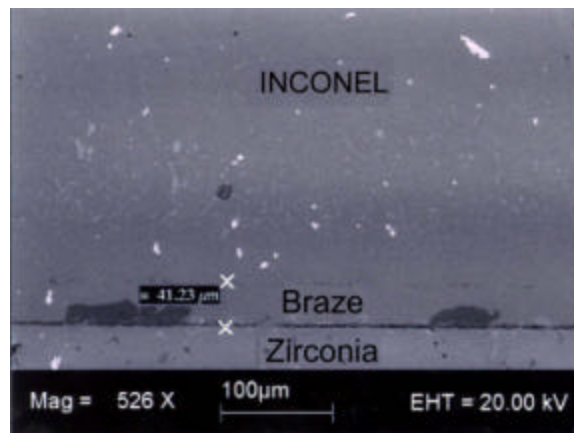


Figure 5: Ti-sputtered zirconia brazed to Inconel using Ni-based brazing alloy

The Ti-O layer was proved to be insoluble in the nickel-based brazing alloy, besides its ability to be wetted by it, forming a relatively stable and strong ceramic/metal interface. This particular characteristic made these layers a natural choice for the experiments conducted with the perovskite substrates.

In those experiments, however, it was observed that the reaction between the ceramic substrate and the brazing alloy were not halted at all. In fact, the nature and morphology of the reaction layers was observed to be the same as that present in previous experiments. As in the previous work, no Fe-segregation was observed. However, localized reduction of the perovskite was evident at the interface with the Ni-based alloy. The next figure and table illustrate the nature and morphology of the reaction products formed:

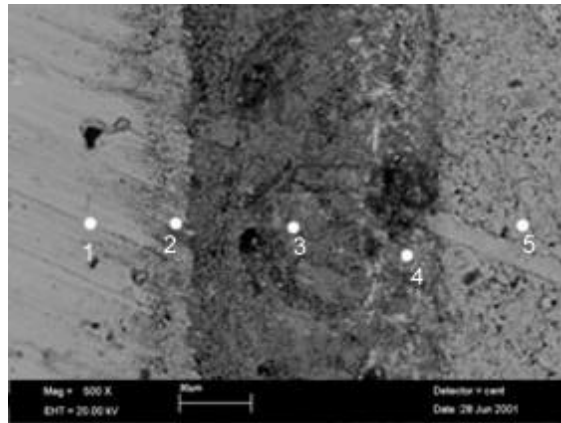


Figure 6: Interface between Perovskite and Ni-based brazing alloy. Ti-based diffusion barrier was used.

	1	2	3	4	5
Ni	80	22	4	1.0	0
Cr	7.2	10.1	3.1	2.1	2.9
Fe	6.1	0.6	8.4	10.2	11
Sr	0	0.8	9.2	11.1	14
La	0	0	2.4	2.5	3.8
O	0	62	72.9	73.1	67
Ti	0.1	0.5	0	0	0
Si	6.6	4	0	0	0

As in the previous experiments, it was observed again that Ni infiltrated the ceramic substrate through the numerous pores present in the system as fabricated. This infiltration, we believe, has several detrimental effects on the strength of perovskite/metal seals:

First, extensive infiltration increases the rate of the reaction between the ceramic substrate and the brazing alloy, exposing more area to the localized reduction that takes place when the Cr contained in the alloy reacts with the perovskite substrate to form Cr_2O_3 or other complex oxides. Additionally, as the infiltrated metal cools down, large thermal stresses build up in the porous area close to the

ceramic/metal interface, due to the different thermal expansion rates of the ceramic and the infiltrated metal.

Despite the fact that Ni-based brazing alloys do not normally dissolve Ti-O layers (as evident from previous experimental results), excessive porosity prevented the Ti-O layer from acting as an effective diffusion barrier. As the infiltrated metal attacked the ceramic immediately below the Ti-O layer, the reactions undergone diminished the adherence of the barrier and further attack was promoted.

Conclusions

From the experiments described above, the following can be concluded:

- The nature and morphological features of the reaction zone differ greatly with the nature of the Perovskite material. In these new experiments no Fe segregation was observed and La-O compounds did not form at the ceramic/braze interface.
- In contrast to the previous experimental evidence, Ni appears to be playing a major role in the decomposition of the ceramic material. The fact that a Ni-Cr-O phase was formed at the interface with the braze, suggests that locally, the oxygen partial pressure was such that decomposition of the ceramic took place.
- The high porosity of the ceramic samples used resulted in high infiltration by the nickel-based brazing alloy. In fact, nickel was observed at depths of 60 microns from the ceramic/braze interface. This infiltration may result in further mechanical damage of the ceramic due to the differences in coefficients of thermal expansion between the nickel alloy and the perovskite matrix. To increase the chances of getting reliable ceramic/metal seals, the porosity of the ceramic substrate must be reduced or an effective diffusion barrier must be implemented.
- For the Ti-O diffusion barriers deposited in the current series of experiments, the same behavior was observed. Therefore, the high porosity of the substrate makes it extremely difficult for diffusion barrier to be effective, since reactions occurring immediately below them tend to detriment the adherence between the layer and the ceramic substrate.
- Further experimentation with diffusion barriers using other materials -probably highly refractory metals or compatible and more stable ceramic oxides- must be done.

- It is believed that the only way to obtain effective perovskite/metal seals is the use of thick diffusion barriers, capable of effectively isolating the ceramic substrate from the attack by the liquid metal. Of course, the nature of the diffusion barrier has to be such that just minimal chemical interaction with the perovskite is likely. It is expected that this is a rather difficult condition to meet.

TASK 3: Determine material mechanical properties under conditions of high temperature and reactive atmosphere

Prof. Sukumar Bandopadhyay and Nagendra Nagabhushana
University of Alaska Fairbanks

Strength of LSFCE tubes in CO₂/CO environment

a) Sample selection and Experimental Procedure

The samples were selected randomly and any dimensional changes in the sample geometry were methodically recorded as outlined in the previous report. The variations in sample dimension used in the present study are as shown in fig.1.

The sample were placed in the autoclave and purged with nitrogen. Purging with nitrogen was done three times and a positive pressure of 25PSI was maintained. The autoclave temperature was raised to 950°C and nitrogen was replaced by CO₂/CO gas mixture. The temperature was then raised to 1000°C and pressure of 25 PSI. The sample was soaked for a period of 15 minutes prior to application of load. Tests were done at 0.5 mm/min as discussed in the previous report

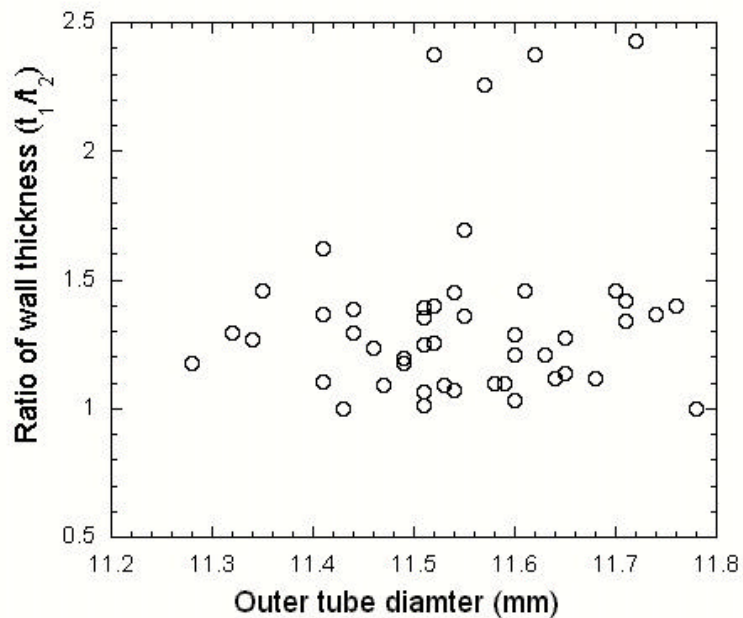


Fig 1. Dimensional variation recorded in the sample set for testing in 90%CO₂/10%CO environment

b) Results:

The fracture strength of the OTM tubes tested in 90%CO₂/10%CO (log P_{O₂} = -12.1) environment was lower than the strength recorded in nitrogen (log P_{O₂} = -4) and are as shown in Table 1. The strength dropped from a maximum of 227 MPa to 166 MPa with increase in reducing condition.

Table 1 : Fracture strength of C-ring specimens in reducing environment

	N ₂ (log P _{O₂} = -4)	90%CO ₂ /10%CO (log P _{O₂} = -12.1)
Minimum Stress, MPa	96.5	70.3
Maximum Stress, MPa	226.7	165.9
Mean Stress, MPa	162.9	108.7
No. of Samples	12	12

The fracture strength plotted as a two-parameter Weibull distribution (Fig. 2) gave a Weibull parameter 'm', of 3.8 and the mean stress as 89 MPa. This was in contrast to the Weibull parameter 'm', of 4.8 and a mean stress of 188 MPa in nitrogen. This implies a considerable drop in the strength values with increasing reducing conditions.

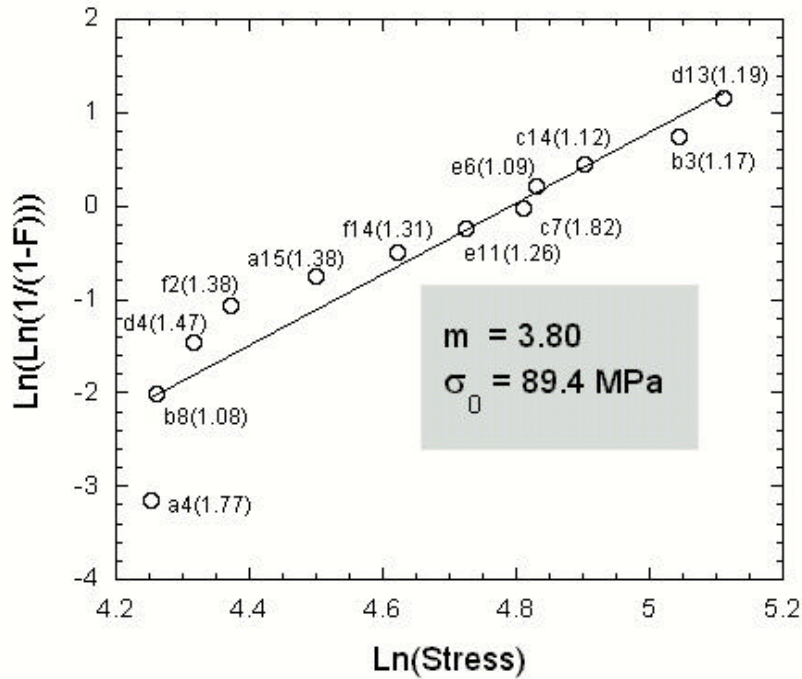


Fig. 2: Weibull distribution of fracture strength in 90%CO₂/10%CO at 1000°C and 0.17 MPa pressure

C) Fracture

The specimens tested failed smoothly at the mid plane on contrast to the tests done in N₂, wherein the sample failed by shattering similar to that observed at room temperature. Fracture in the specimens was by brittle cleavage. Microscopic analysis indicated strength distribution to be controlled by both surface and volume flaws. However, fracture was seemingly controlled by volume relate process flaws. Microscopic fracture typically indicated pores at grain-boundary triple points and grain-boundary cavitations associated with high temperature fracture.

An interesting factor observed in fracture was the absence of well defined relief between the grain boundaries and the grain as observed in samples fractured in N₂ (log P_{O2} = -4). A lower magnification of fracture (Fig 3 a) indicates spherules in the grains and although the grain boundaries are still marked, there is no visible contrast between them. A line scan profile (Fig .4a) of the elements across the fractured surface indicated that the Sr and Fe are the dominating elements in the Fracture.

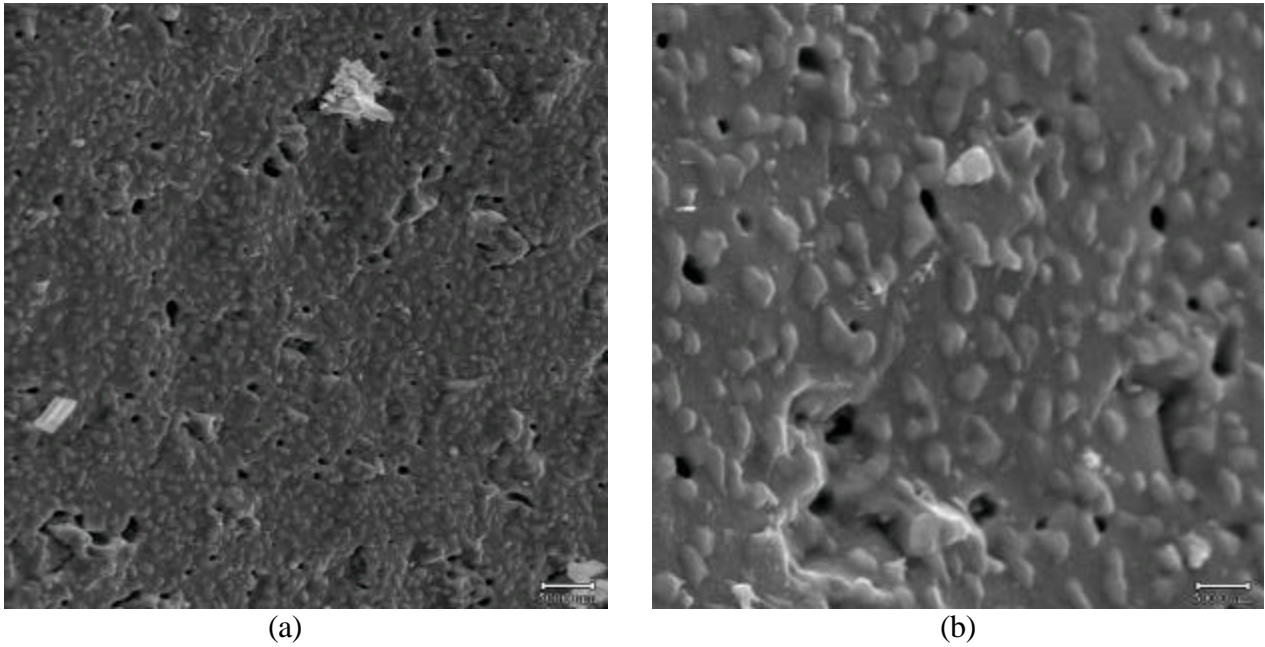


Fig 3: Fracture morphology observed in sample tested in a CO_2/CO at : a) Low magnification and b) High magnification

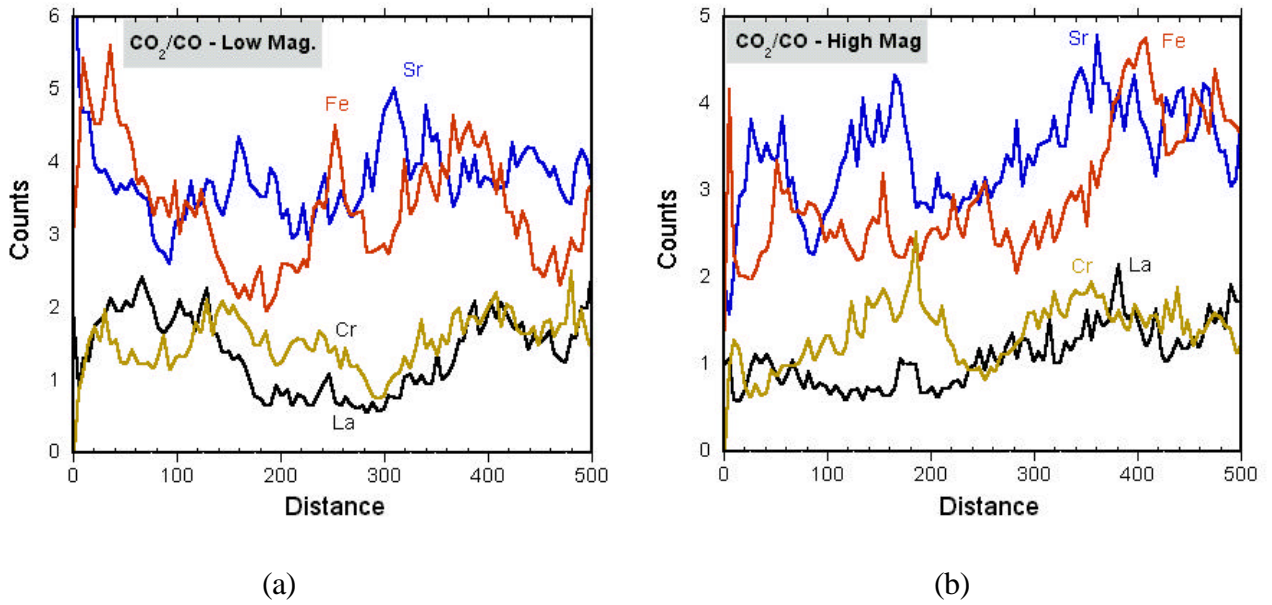


Fig. 4 Line Scan profile of elements in fractured grains at : a) Low magnification and b) High magnification

At higher magnification (Fig. 3b), the spherules in the grains are very clearly visible. There was no apparent orientation of the spherules in the individual grains. Also, the grain boundaries though visible showed no distinct change in morphology. The line scan profile (Fig. 4b) indicated that the spherules were rich in La, Sr, Fe, Cr elements as compared to the matrix. This possibly implies that a new phase with a different structure could be forming from the matrix. However, the exact composition of the spherule phase could not be determined.

Future Work

Extensive microscopic studies are planned to determine the elemental distribution across fractured grains and also the phases formed on the application of any stress. Studies are also planned to determine strength of the OTM in a more reducing condition (10% CO₂/90% CO).

Task 4: Preparation and Characterization of Dense Ceramic Oxygen Permeable Membranes

By: Professor Harlan Anderson, University of Missouri-Rolla

Preparation and Characterization of $\text{La}_{1-x}\text{FeO}_{3-d}$

By: Xiao-Dong Zhou

1. Introduction

The perovskite series of $\text{La}_{1-x}\text{Sr}_x\text{FeO}_{3-d}$ ($0 < x < 1$, later referred as LSF series) was first studied by Waugh in 1960¹, and a structure change was observed from orthorhombic at low x to cubic at $x=1$. Besides the structure evolution, which was extensively studied by Dann et al.², the series of $\text{La}_{1-x}\text{Sr}_x\text{FeO}_{3-d}$ is attractive since the valence state of Fe changes with the value of x , which results in the complex magnetic properties³. As far as electrical property is concerned, LSF series are considered as a mixed ionic and electronic conductor (MIEC) candidate, however, surprisingly there were not enough references that could support this assumption. In this paper, the formation of LSF was processed with liquid phase method and the perovskite phase transition was investigated at various calcinations temperatures. Sintering and electrical properties were studied for some x values and the full investigation of all x values will be fulfilled later.

2. Experimental

2.1. Precursor solution preparation and standardization

Lanthanum nitrate ($\text{La}(\text{NO}_3)_3$), strontium nitrate ($\text{Sr}(\text{NO}_3)_2$) and iron nitrate ($\text{Fe}(\text{NO}_3)_3$) were supplied from Aldrich with the of 99.9% except iron source has the purity of 99%. Those nitrates were dissolved into purities water and thermogravimetry method was used to standardize those solutions. Five specimens in crucibles were used for each solution. After slowly drying, those crucibles were put into an electric furnace and calcined at 800°C . Upon the furnace cooling down around 100°C , quickly transfer those crucibles to dessiccator and measure the weight loss.

2.2. Powder formation and Characterization

A mixture of nitrate solutions, citric acid and glycerin (or ethylene glycol) was heated to form a polymeric solution precursor, which was transferred to the resin type of gel. The gel was heated at 300°C for 1 hour and then pulverized into powders, which were calcined at various temperatures.

Phase purity and crystalline structure were studied by powder X-ray diffraction (XRD, Scintag 2000) using Cu Ka source with Ni as filter. Powder morphology was examined by scanning electron microscopy (SEM, Hitachi and JEOL) and the specific surface areas (SSA; m^2/g) of powders were measured by the Brunauer-Emmett-Teller (BET) method (Quantachrome; Nova 1000). From the SSA data, the particle size (d_{BET} , μm) was calculated by $d_{\text{BET}} = 6/(\rho \cdot \text{SSA})$, where ρ is the density of the powders (g/cm^3). The influence of annealing temperature on the powder characteristics was determined. Bar shaped specimens (3.8 cm x 1.25 cm) were prepared for electrical measurements by uniaxial-pressing at 40 MPa, followed by cold isostatic pressing at 310 MPa. To minimize impurity levels no binder was used in the pressing step. Bars were sintered on LSF substrates of the same composition at temperatures ranging between 1000 to 1400°C, with a heating rate of 3°C/min and a soak time of 4 h. Scanning electron microscopy (Hitachi S-4700 and JEOL T330A, SEM) was used to investigate the raw materials and sintered ceramics. Sintering density was measured by Archimedeian method using kerosene as the liquid medium.

2.3. Electrical property measurement

Four-point dc and two-point ac impedance spectroscopy (IS) measurements were performed using a Solartron 1260 frequency response analyzer with a 1296 interface, with an applied voltage of 0.01V over a frequency range of 1Hz to 1MHz. Thick film Pt electrodes were used for all measurements. Data were collected for temperatures ranging between 300 and 800°C. All electrical measurements were performed only after a stable value of the dc conductivity was achieved. Z-plot software (Scribner Associates Inc.) was used to develop appropriate equivalent circuits for modeling the impedance data.

3. Results and Discussion

3.1. Formation of the perovskite phase

Citric acid ($\text{C}_6\text{H}_8\text{O}_7$, Figure 1), ethylene glycol ($\text{C}_2\text{H}_6\text{O}_2$, Figure 1) and glycerin ($\text{C}_3\text{H}_8\text{O}_3$, Figure 1) were widely used as the precursors to form oxide powders. Figure 1 shows their molecular structure and the possible reactions. The compositions studied in this paper are shown in Table 1, in which the specific surface area, sintering density and temperature are also included. The typical composition is $\text{La}_{0.6}\text{Sr}_{0.4}\text{FeO}_3$ with the citric acid and ethylene glycol as precursors. Figure 2 shows the x-ray diffraction of the powders calcined at different temperatures. The major perovskite phase was formed under the calcinations temperature of 600°C, at which the specific surface area of the calcined

powders reached the maximum value, which is shown in Figure 3. SEM images of the calcined powders are shown in Figures 4-8.

Table 1. Specimen compositions and properties of $\text{La}_{1-x}\text{Sr}_x\text{FeO}_3$ series in this paper.

(The ratio of chelatant over all cations is 1:1)

X	Phase ($T_c=600^\circ\text{C}$)	$\rho_{\text{sintering}}$	SSA ($T_c=600^\circ\text{C}$)	
0.1	Pure Perovskite			
0.2	Pure Perovskite	> 95%	12.0 m^2/g	
0.4	Pure Perovskite	> 95%	11.8 m^2/g	
0.6	Pure Perovskite	> 98%	12.1 m^2/g	
2/3	Pure Perovskite			

The citric acid method (Pechini method) is quite complicated, and it has many changeable experimental variables that affect the final product, including the ratio of citric acid vs. ethylene glycol, the ratio of chelatant over cations, the composition of chelatants, drying temperature and calcination temperature. In this paper, the chelatant composition, calcination temperature and ratio of chelatant over cations were studied. The as-synthesized powders were stick at both poles of magnetic stir bar in a specific ordering, which obviously showed that those powders were magnetic. After calcined at 400°C and 500°C , the powder was dark brown and changed to black under 600°C , at which the perovskite phase was formed from XRD results. Hence, those dark brown powders are possible oxide mixture (cation segregation), in which Fe oxide mostly contributed to the dark brown color. However, the segregation was controlled in the small range ($< 50\text{nm}$) so that the perovskite phase could be achieved at 600°C . This temperature was normally around 800°C when mixtures of lanthanum, strontium and iron oxides were used. The small range ($\sim 50\text{nm}$) was determined from XRD line broadening, which revealed that the smallest crystalline particle was less than 50nm .

The particle size was decreased as increasing the ratio of chelatant over all cations (shown in Figure 9 to Figure 12).

3.2. Sintering and microstructure

SEM image of sintering $\text{La}_{0.6}\text{Sr}_{0.4}\text{FeO}_3$ 1300°C for 4 hours is shown in Figure 13; the high sintering density (> 98%) is undoubtedly due to the high surface area ($\sim 12 \text{ m}^2/\text{g}$) of the green powders. The sintering behavior of other LSF series is similar to this.

3.3. Electrical Properties

3.3.1. The influence of measuring temperature

Figure 14 and Figure 15 shows the $\ln(\sigma T)$ vs. $10000/T$ of $\text{La}_{0.6}\text{Sr}_{0.4}\text{FeO}_3$ and $\text{La}_{0.6}\text{Sr}_{0.4}\text{Fe}_{0.85}\text{Ga}_{0.15}\text{O}_3$ at various atmosphere. The maximum of conductivity is possibly due to ionic compensation by oxygen vacancy formed at high temperature. In accordance with Kroger-Vink notation, doped with Sr will result in either holes (h°) or oxygen vacancies ($\text{V}_\text{O}^{\circ\circ}$); the holes are likely dominated. At high temperature, loss of oxygen will generate oxygen vacancy, which compensates the hole concentration, i.e. decreases the conductivity by:

$$[\text{Sr}_{\text{La}}'] = [\text{h}^\circ] + 2[\text{V}_\text{O}^{\circ\circ}].$$

For each $\text{V}_\text{O}^{\circ\circ}$ generated in the lattice, two p-type carriers (h°) are eliminated. The more detailed information will be given with the Seebeck data.

3.3.2. The influence of oxygen partial pressure.

Figure 16 and Figure 17 are $\log(\sigma)$ vs. $\log(p\text{O}_2)$ for $\text{La}_{0.6}\text{Sr}_{0.4}\text{FeO}_3$ and $\text{La}_{0.6}\text{Sr}_{0.4}\text{Fe}_{0.85}\text{Ga}_{0.15}\text{O}_3$ at different temperatures. No significant changes took place by replacing of Fe with Ga, which may due to the same valence state of Ga (3+) and Fe (3+) and the Ga^{3+} could stabilize the Fe^{3+} , so that the conductivity, especially the ionic contribution did not change very much. Another interesting phenomenon here is the 1/6 slope over the range of $p\text{O}_2 > p\text{O}_2^*$ at various temperatures. The 1/4 should be normally observed for acceptor-doped oxide. Again the detailed explanation will be given by combining with Seebeck data.

Figure 18 and Figure 19 are the normalized electron and hole contribution to total conductivity for $\text{La}_{0.6}\text{Sr}_{0.4}\text{FeO}_3$ and $\text{La}_{0.6}\text{Sr}_{0.4}\text{Fe}_{0.85}\text{Ga}_{0.15}\text{O}_3$ by the applying the equation:

$$\sigma = \sigma_e^0 p\text{O}_2^{-1/6} + \sigma_h^0 p\text{O}_2^{-1/6}$$

where the σ_e^0 denotes the temperature dependant electron conductivity and σ_h^0 is the temperature dependant hole conductivity.

4. Future work

- Study the effect of chelant on the particle size and morphology and investigate the particle formation mechanism
- Investigate the microstructure evolution of LSF series and examine the crystal structure
- Fulfill Seebeck measurements and study the pO_2 dependant conductivities
- Supply samples to Yang with the composition of $La_{1/3}Sr_{2/3}FeO_3$ at various atmosphere quench.
- Finish pure CeO_2 conductivity measurements (close to finish) and investigate the grain boundary effect on undoped CeO_2 electrical properties.

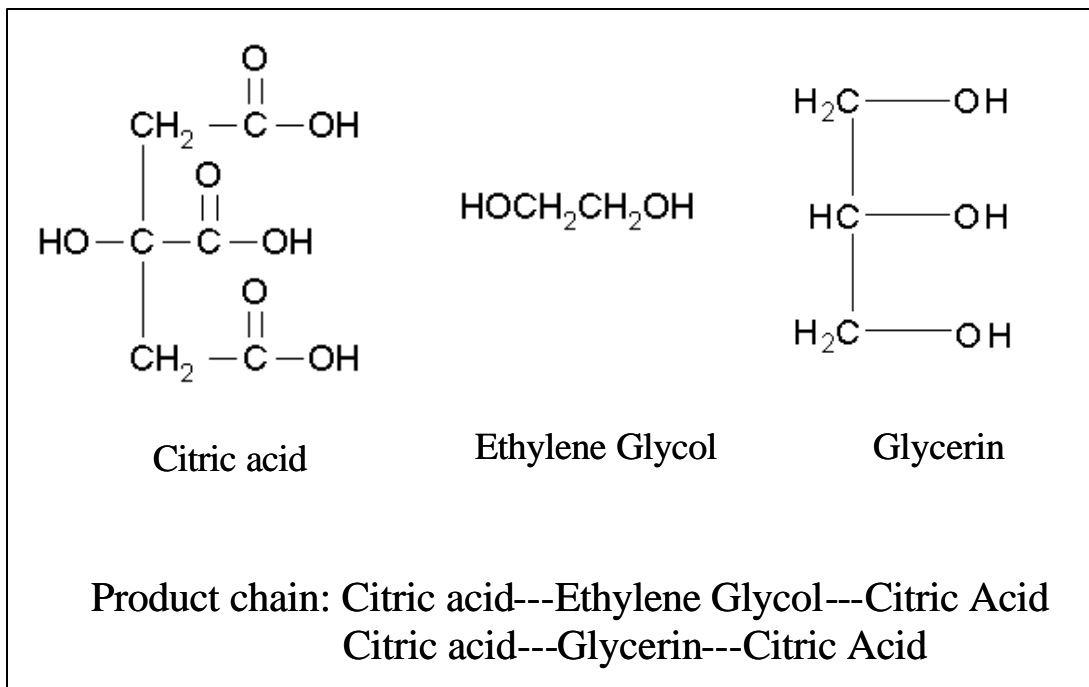


Figure 1. Molecular structure of citric acid, ethylene glycol and glycerin and the possible product chains.

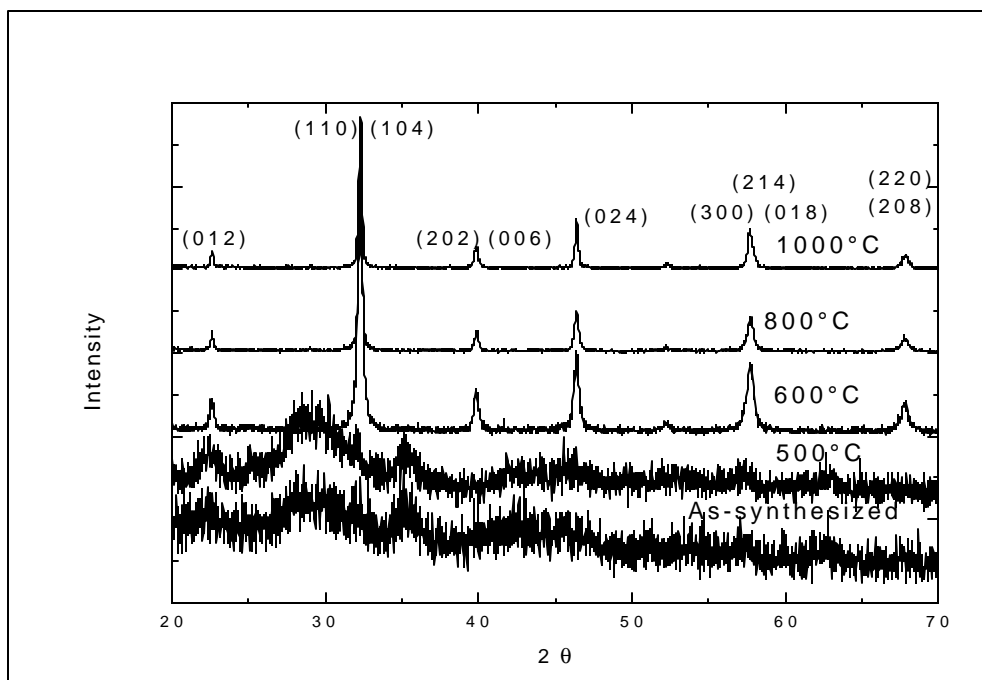


Figure 2 (a). X-ray diffraction of $\text{La}_{0.6}\text{Sr}_{0.4}\text{FeO}_3$ powders calcined at various temperatures.

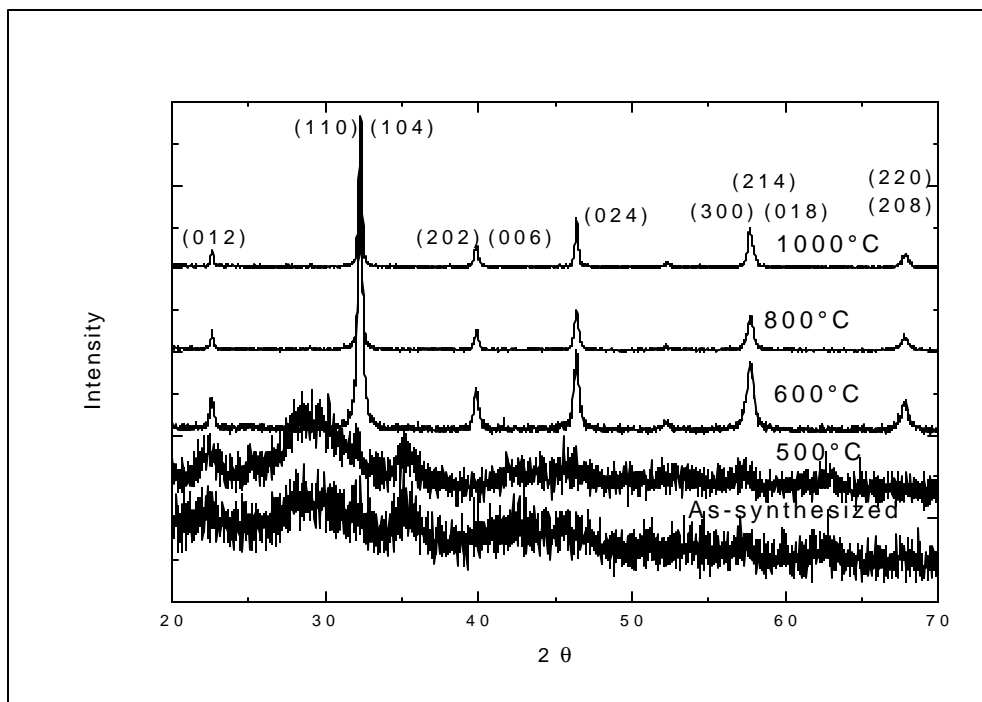


Figure 2 (b). X-ray diffraction of $\text{La}_{0.6}\text{Sr}_{0.4}\text{FeO}_3$ powders calcined at various temperatures.

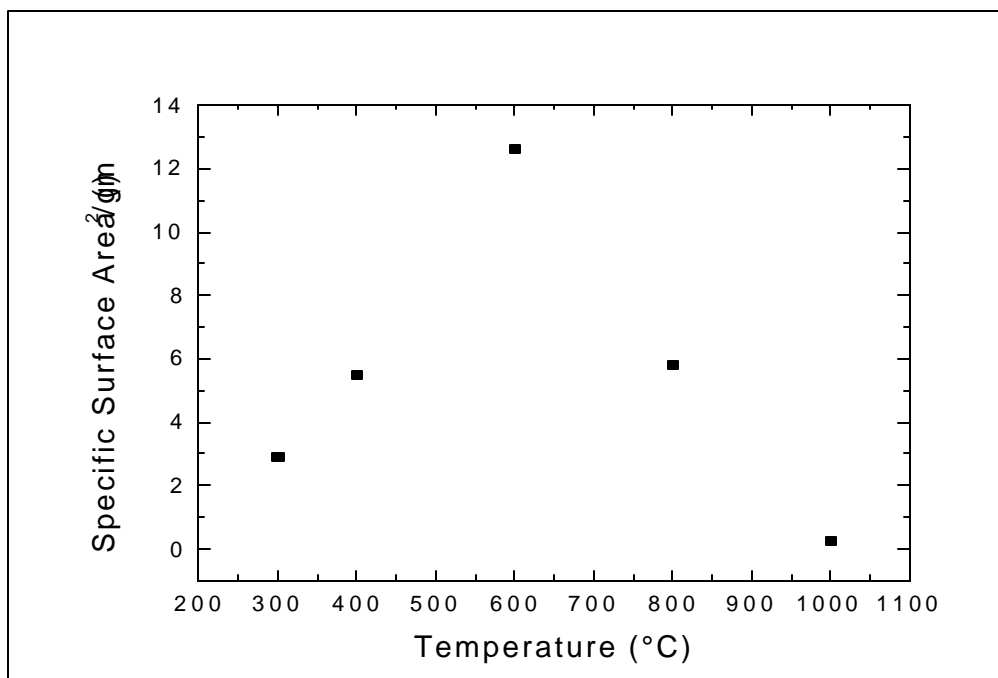


Figure 3. Specific surface area of calcined powders at different temperatures for the composition of La_{0.6}Sr_{0.4}FeO₃.

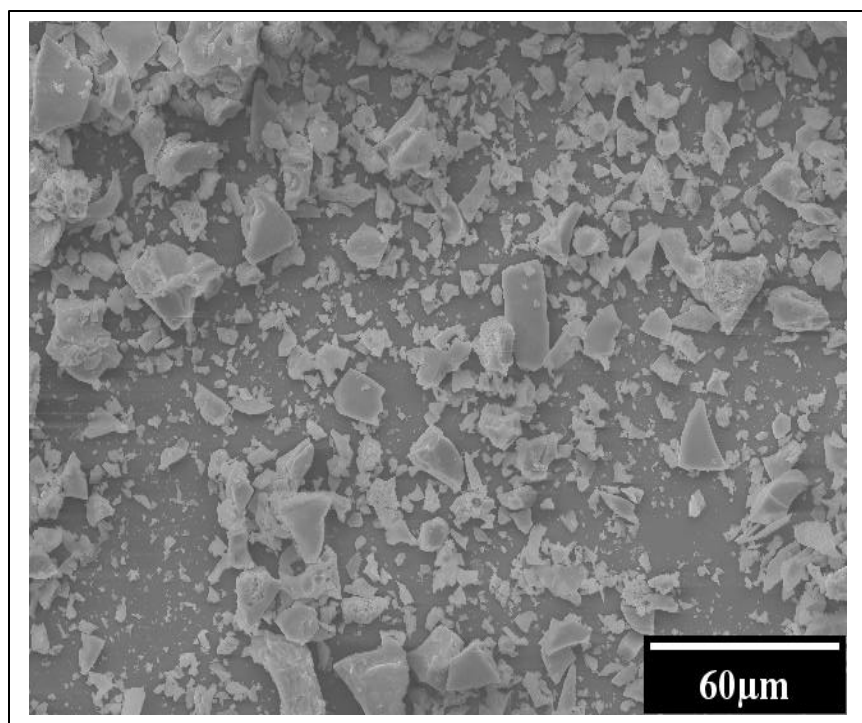


Figure 4. SEM image of La_{0.6}Sr_{0.4}FeO₃ calcined at 500 °C for 1 hour.

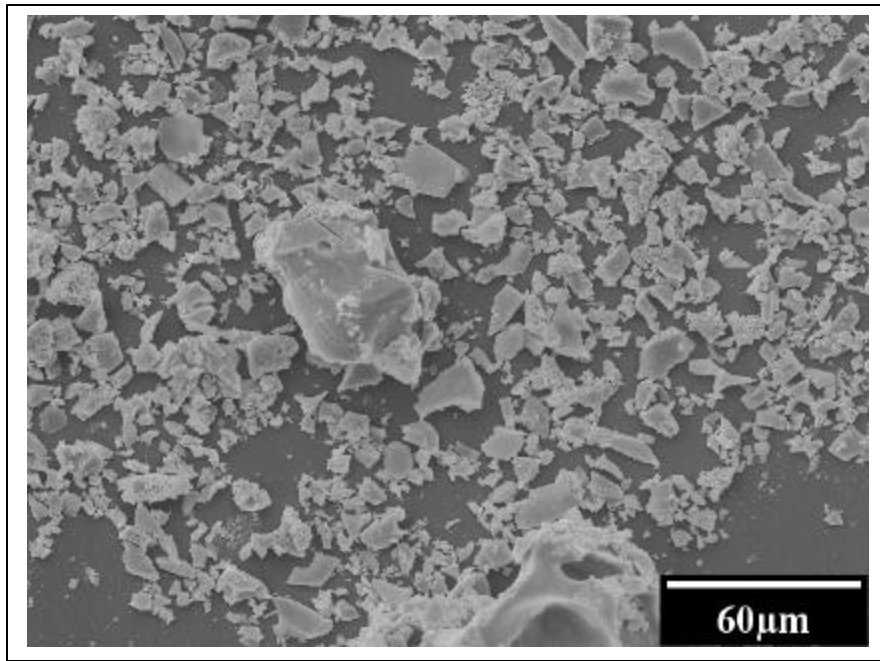


Figure 5. SEM image of $\text{La}_{0.6}\text{Sr}_{0.4}\text{FeO}_3$ calcined at 600°C for 1 hour.

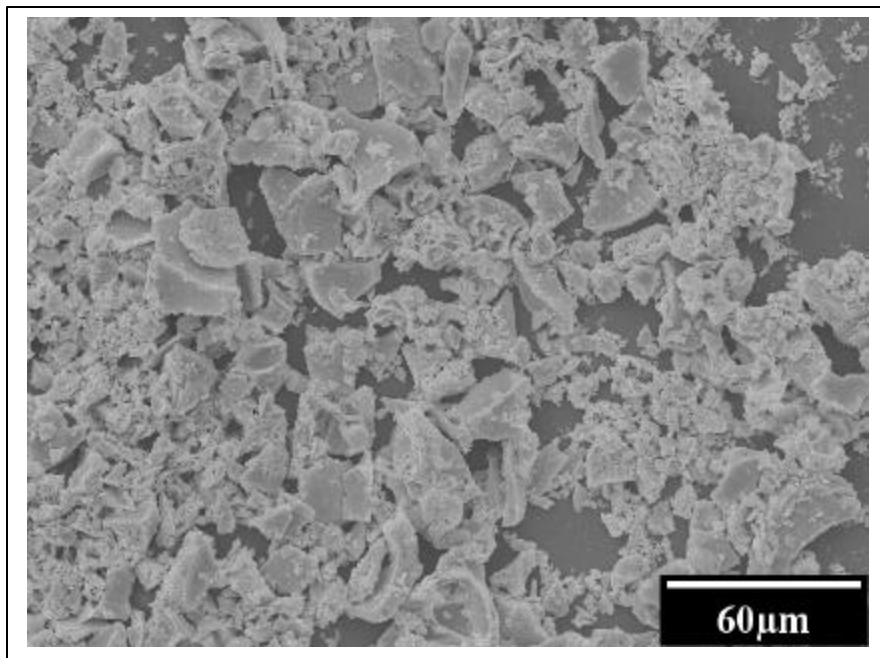


Figure 6. SEM image of $\text{La}_{0.6}\text{Sr}_{0.4}\text{FeO}_3$ calcined at 800°C for 1 hour.

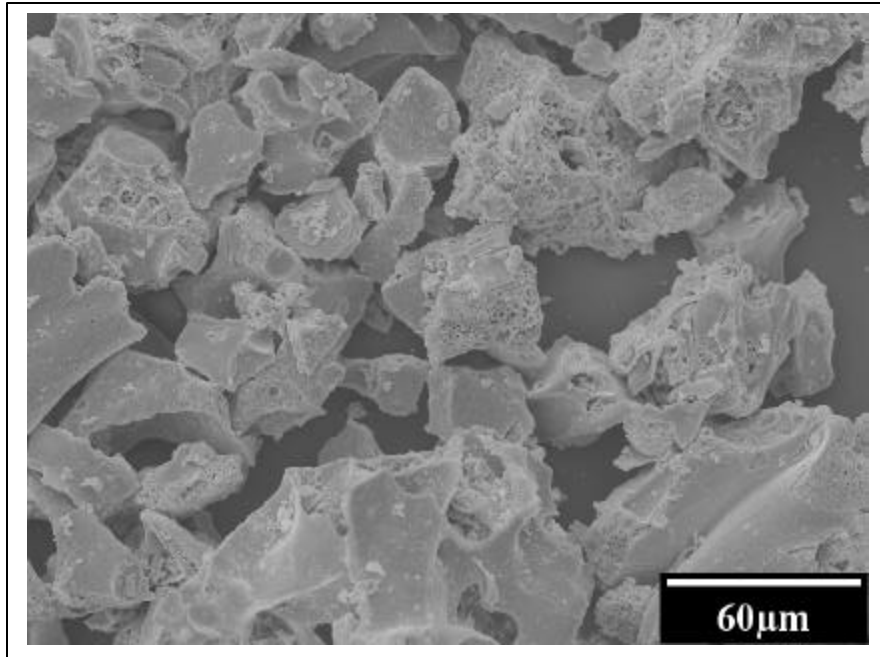


Figure 7. SEM image of $\text{La}_{0.6}\text{Sr}_{0.4}\text{FeO}_3$ calcined at 1000°C for 1 hour.

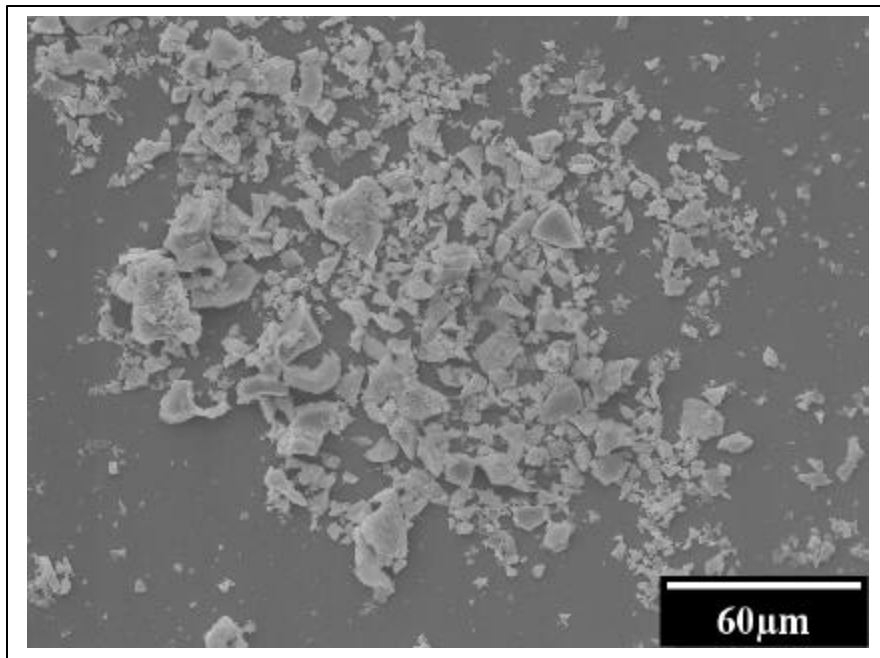


Figure 8. SEM image of $\text{La}_{0.6}\text{Sr}_{0.4}\text{FeO}_3$ as-synthesized powders.

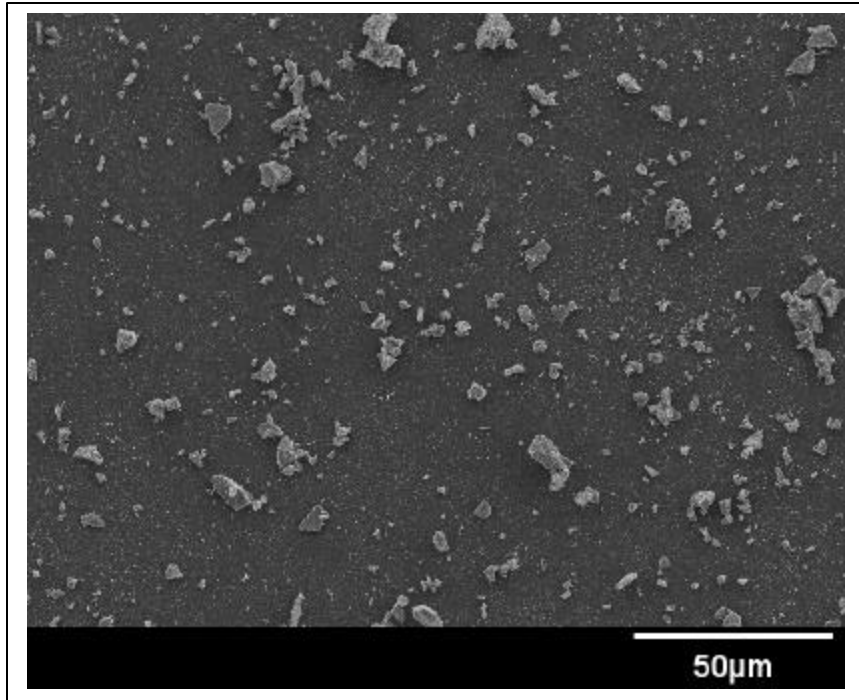


Figure 9. SEM image of $\text{La}_{0.8}\text{Sr}_{0.2}\text{FeO}_3$ calcined at 600°C for 1 hour. (Citric acid-glycerin/all cations = 2:1).

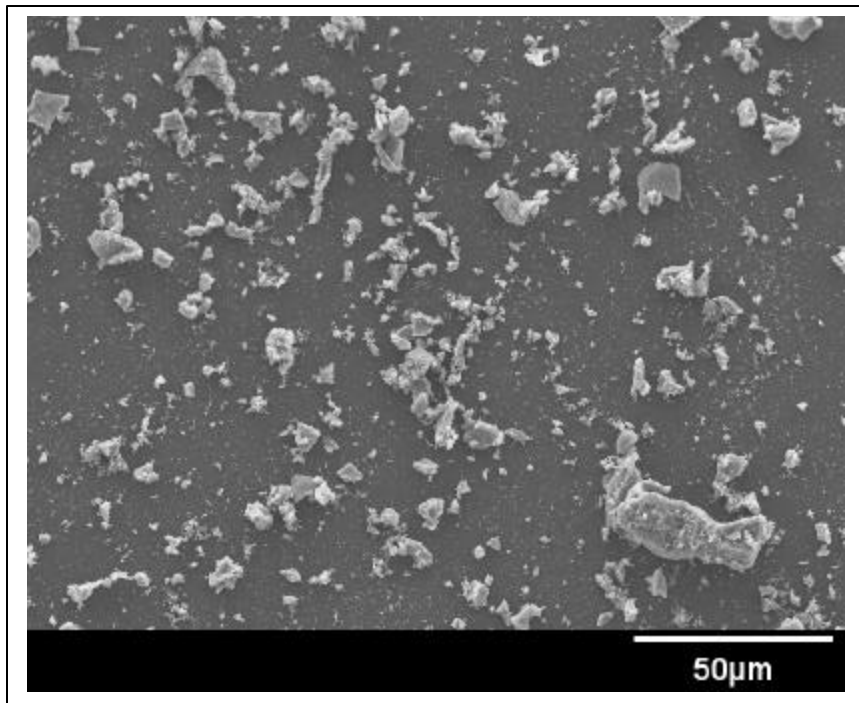


Figure 10. SEM image of $\text{La}_{0.8}\text{Sr}_{0.2}\text{FeO}_3$ calcined at 600°C for 1 hour. (Citric acid-ethylene glycol/all cations = 2:1).

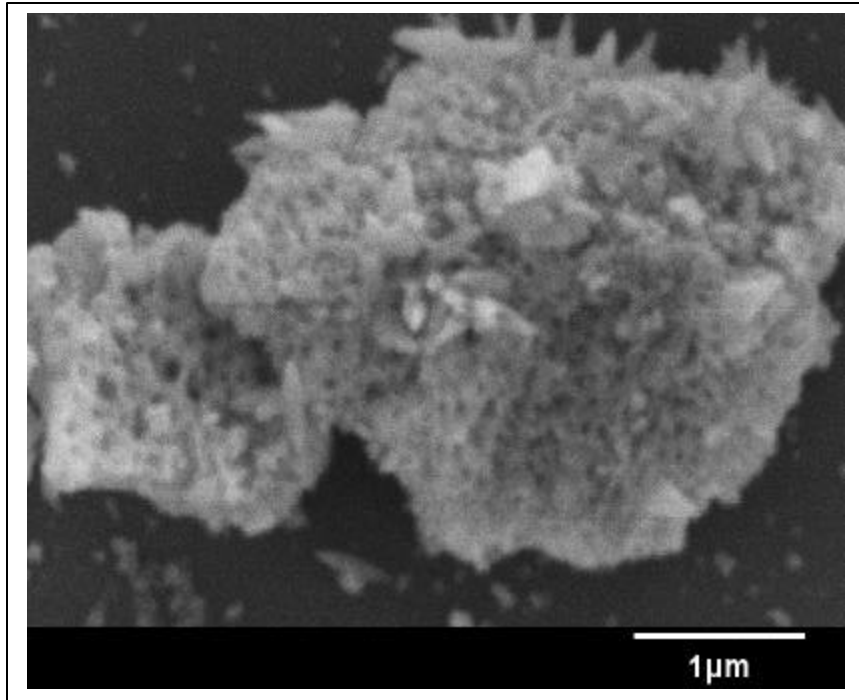


Figure 11. High magnification SEM image of $\text{La}_{0.8}\text{Sr}_{0.2}\text{FeO}_3$ calcined at 600°C for 1 hour. (Citric acid-glycerin/all cations = 2:1).

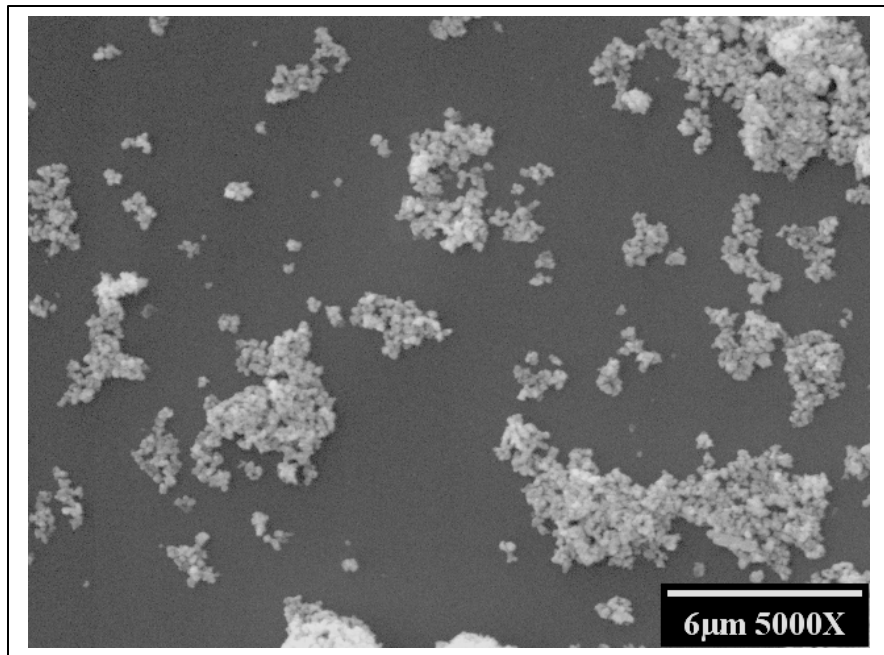


Figure 12. SEM image of $\text{La}_{0.9}\text{Sr}_{0.1}\text{FeO}_3$ calcined at 600°C for 1 hour. (Citric acid-glycerin/all cations = 3:1).

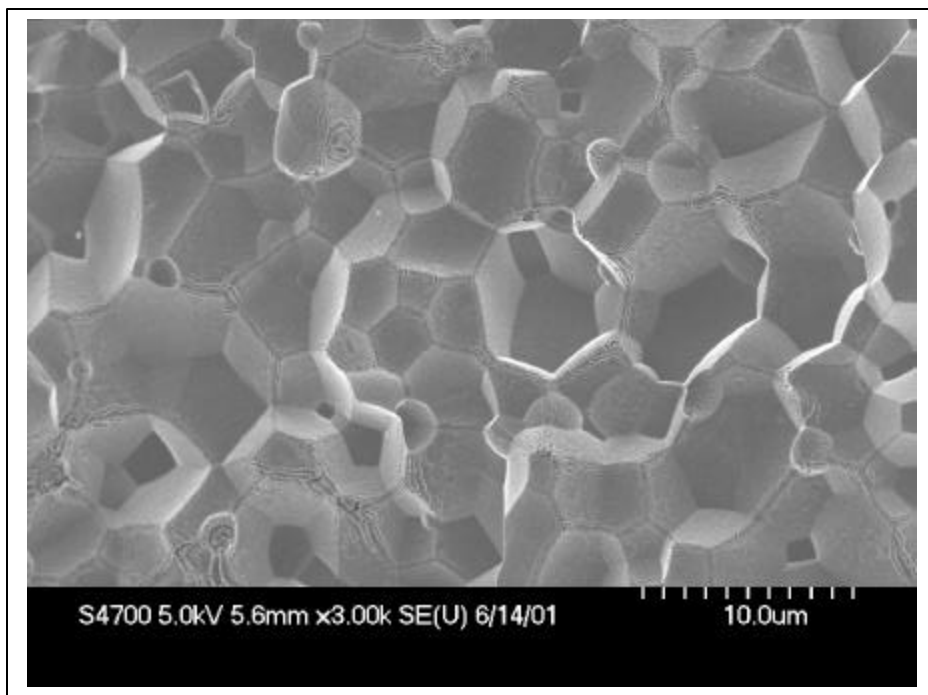


Figure 13. SEM image of $\text{La}_{0.6}\text{Sr}_{0.4}\text{FeO}_3$ sintered at 1300°C for 4 hours.

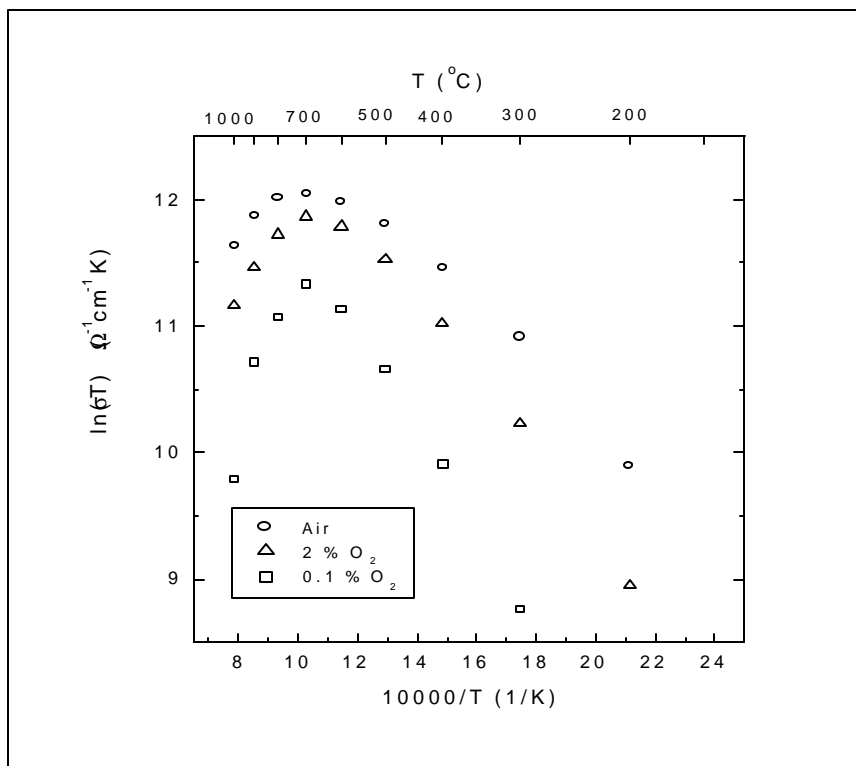


Figure 14. $\ln(\sigma T)$ vs. $10000/T$ for $\text{La}_{0.6}\text{Sr}_{0.4}\text{FeO}_3$ at different atmosphere.

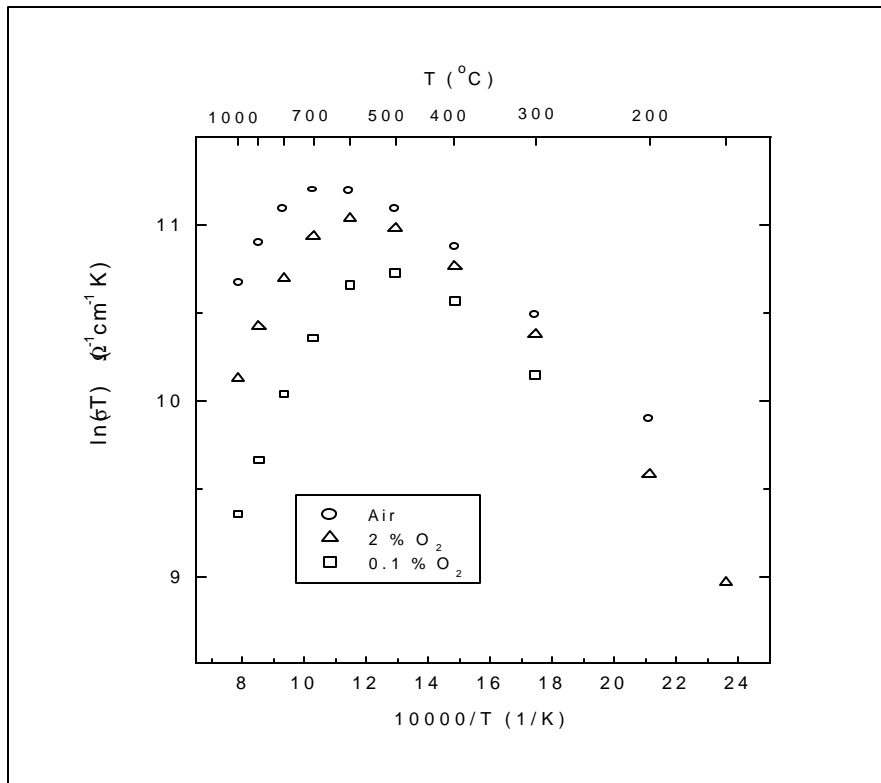


Figure 15. $\ln(\sigma T)$ vs. $10000/T$ for $\text{La}_{0.6}\text{Sr}_{0.4}\text{Fe}_{0.85}\text{Ga}_{0.15}\text{O}_3$ at different atmosphere.

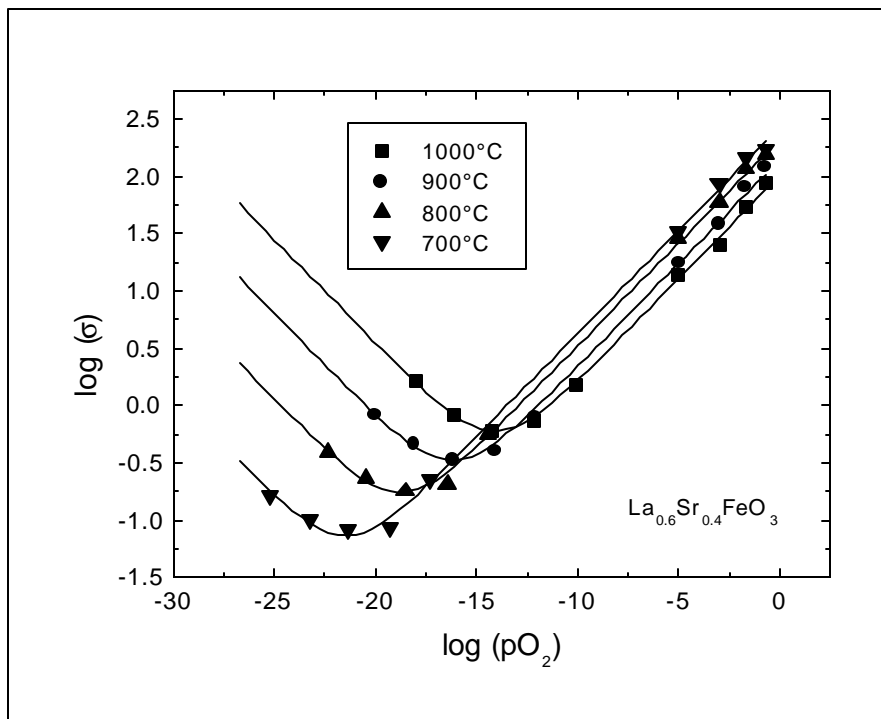


Figure 16. $\log(\sigma)$ vs. $\log(p\text{O}_2)$ for $\text{La}_{0.6}\text{Sr}_{0.4}\text{FeO}_3$ at different temperatures.

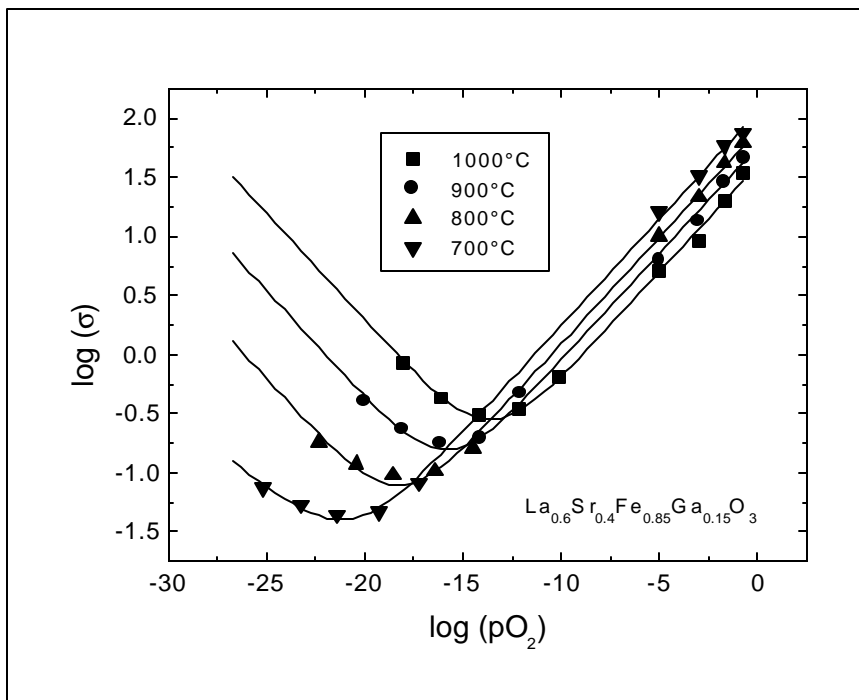


Figure 17. $\log(\sigma)$ vs. $\log(pO_2)$ for $La_{0.6}Sr_{0.4}Fe_{0.85}Ga_{0.15}O_3$ at different temperatures.

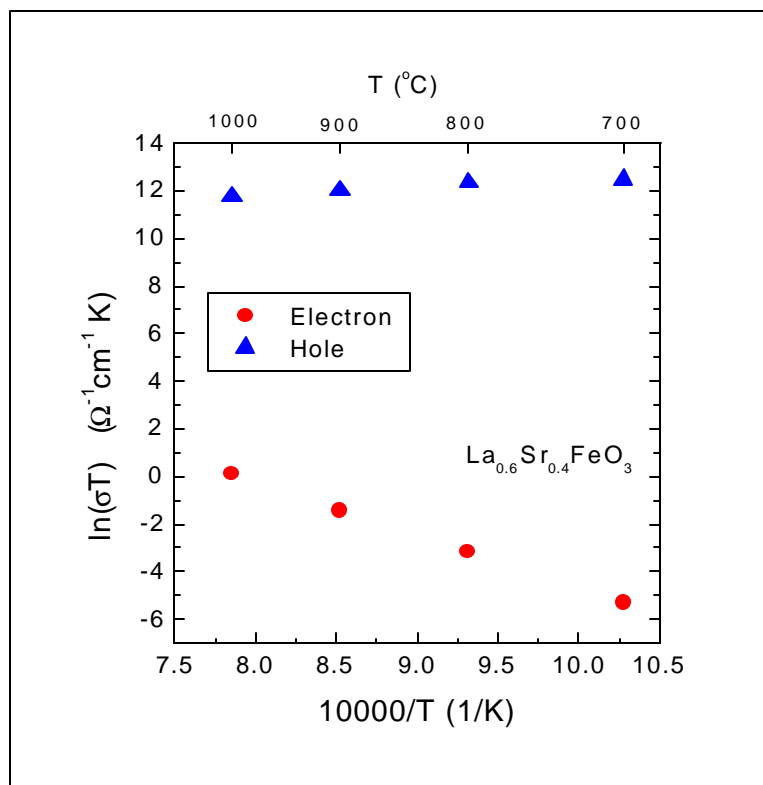


Figure 18. Normalized electron and hole contribution to total conductivity for $La_{0.6}Sr_{0.4}FeO_3$ vs. $10000/T$.

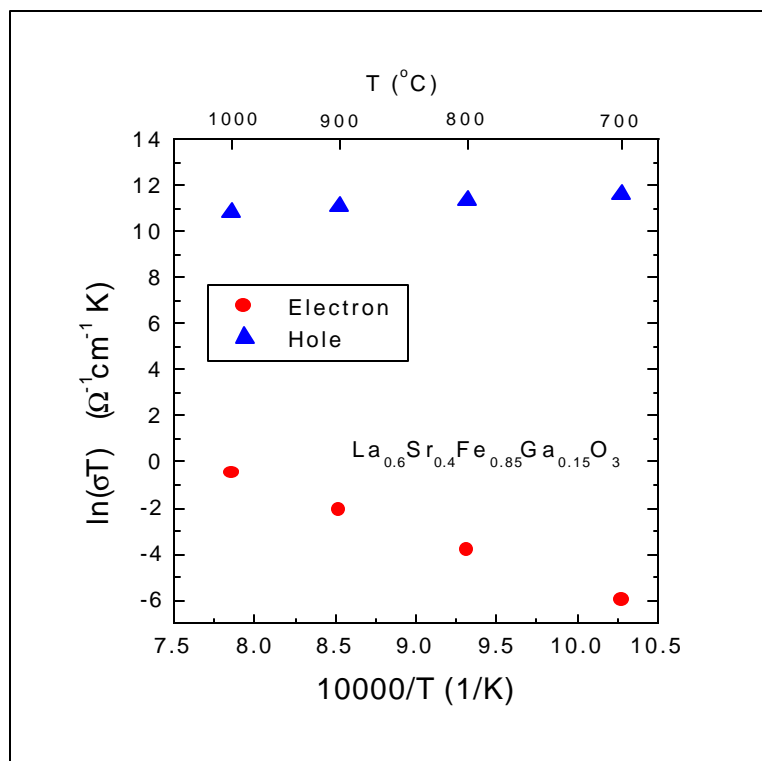


Figure 19. Normalized electron and hole contribution to total conductivity for $\text{La}_{0.6}\text{Sr}_{0.4}\text{Fe}_{0.85}\text{Ga}_{0.15}\text{O}_3$ vs. $10000/T$.

Crystal Structure, Magnetic Properties and Mössbauer Studies of the $\text{La}_{0.6}\text{Sr}_{0.4}\text{FeO}_{3-\delta}$ Prepared by Quenching in Different Atmospheres

J. B. Yang, W. B. Yelon, and W. J. James
 Graduate Center for Materials Research and Departments of Chemistry
 Physics, University of Missouri-Rolla, Rolla, MO 65409

Z Chu
 Department of Physics, University of Missouri-Columbia, Columbia, MO
 65211

1. Abstract

Samples of $\text{La}_{0.6}\text{Sr}_{0.4}\text{FeO}_{3-\delta}$ compounds prepared by quenching in different gaseous environments were studied by x-ray diffraction, neutron diffraction, magnetization measurements, and Mössbauer spectroscopy (MS). Oxygen vacancies were determined from the iodometric techniques as well as the neutron diffraction studies. All materials are single phase and crystallize in the hexagonal perovskite structure. Samples prepared in flowing air, N_2 , and O_2 yielded oxygen vacancies ranging

from 0 to 3%. The oxygen vacancy concentration increases from 7.2% to 8.8% as the ratio of CO/CO₂ changes from 10:90 to 90:10. The air-, N₂- and O₂-quenched samples have a magnetic ordering temperature (Néel temperature) in the range of 300-325 K. The Néel temperature increases to 800 K for all the samples subjected to the reducing atmosphere CO/CO₂. The neutron data refinements and magnetization data indicate that the Fe sublattice of La_{0.6}Sr_{0.4}FeO_{3-δ} has an antiferromagnetic structure below the Néel temperature. The Fe atoms possess a magnetic moment of 3.8 μ_B and a hyperfine field of 52 T in the CO/CO₂ quenched samples. It is found that the heat treatment in the CO/CO₂ atmosphere creates more oxygen vacancies, increases the Fe³⁺ ion concentration, and the unit cell volume. However, the Fe-O bond length remains nearly constant, resulting in distortion/rotation of the oxygen octahedra which increases the Fe-O-Fe bond angle as much as 12 degrees. This dramatically affects the Fe-O-Fe super-exchange coupling. The change of the Fe-O-Fe bond angle and the increase of Fe³⁺ ions in the CO/CO₂ heat treatment play a key role in the increase of the Néel temperatures, magnetic moments, and the hyperfine fields in these compounds. Therefore by creating oxygen vacancies or having excess oxygen, the exchange interaction of Fe-O-Fe is affected, and leads to large changes in the magnetic properties, such as the Néel temperature, the magnetic moments and the hyperfine interactions in the perovskite structure.

PACS numbers: 75.60, 75.30, 75.10, 81.40

1. Introduction

There has been a great deal of contemporary interest in perovskite compounds of the type ABO_{3-δ}, where A is La or Sr, B is a 3d transition metal such as Fe, Mn, Co and Ni. In particular, the Fe and Mn compounds have been extensively studied as regards their magnetic and transport properties. The perovskites have a wide homogeneity range as far as oxygen content is concerned. Mixed valence of the transition metal ions can be induced in these compounds by introducing divalent ions such as Ba, Ca and Sr at the trivalent La site or by creating oxygen vacancies. The magnetic properties of these compounds are thought to arise from a superexchange mechanism involving 3d electrons of the transition metal ions and oxygen p orbitals. Thus oxygen plays a very important role in magnetic ordering of these compounds. Some perovskite-type La_{1-x}Sr_xBO_{3-δ}(B=Mn,Fe,Co) compounds are strongly covalent antiferromagnetic metals while others are metallic with an enhanced Pauli paramagnetism and many are magnetic insulators. For example, La_{1-x}Sr_xMnO_{3-δ} and La_{1-x}Sr_xFeO_{3-δ} become ferromagnetic for x>0.05 and metallic for x≤0.2 due to hole doping [1-4]. La_{1-x}Sr_xFeO_{3-δ} does not exhibit either a magnetic or an electronic transition [5]. LaFeO₃ is an antiferromagnetic insulator

and has an orthorhombically distorted perovskite structure. Upon substituting Sr^{2+} for La^{3+} , the orthorhombic structure becomes pseudocubic for $x \leq 0.4$ in $\text{La}_{1-x}\text{Sr}_x\text{MnO}_{3-\delta}$. As for $x > 0.4$, the Fe^{4+} content decreases markedly due to oxygen loss, resulting in the actual Fe^{4+} content having a maximum of about 40% for $x=0.5$ [5]. When Sr^{2+} is substituted for La^{3+} , the activation energy of the semiconducting compounds and the antiferromagnetic Néel temperature decrease systematically [5-6]. There are some characteristics of the $\text{La}_{1-x}\text{Sr}_x\text{BO}_{3-\delta}$ compounds which provide the potential for technical applications: (a) mixed valence states of the 3d transition metals on the B sites which results in a high electronic conductivity, (b) large oxygen nonstoichiometry which is related to the high diffusivity of the oxide ions, and (c) formation of a solid solution with a wide miscibility range. Thus these compounds have application as catalysts, chemical sensors, electrodes and solid electrolyte fuel cells. Recently, a colossal magnetoresistance has been found in the perovskite manganites $\text{La}_{1-x}\text{Sr}_x\text{MnO}_{3-\delta}$, and a structural modulation accompanying the charge ordering transition has been confirmed by electron microscopy [7]. The modification of the chemical composition on the perovskite A sites and the concentration of the oxygen vacancies is effective for controlling the crystal structure and fundamental physical properties of the perovskite-type compounds [8]. Previous studies [9] suggest that the structure and magnetic properties are strongly dependent on the heat treatment.

In this study, we report on the structure, magnetic properties, and the Mössbauer spectra of the $\text{La}_{0.6}\text{Sr}_{0.4}\text{Fe}_{3-\delta}$ compounds prepared by varying heat treatment. The dependence of the structure, magnetic properties and hyperfine interaction on the heat treatment environments, has been studied in detail. The dependence of the exchange coupling on the oxygen vacancy concentration and the structure has been investigated by analyzing the experimental data. The oxygen vacancy concentration and the ratio of $\text{Fe}^{3+}/\text{Fe}^{4+}$ ions have been determined by neutron diffraction and Mössbauer spectra. A marked increase of the Néel temperature, magnetic moments, and hyperfine field observed for the CO/CO_2 treated samples is explained on the basis of the super-exchange coupling bond distances and angles between the Fe-O-Fe linkage.

2. Experimental Methods

The liquid-mixing method [10-11] was used to prepare $\text{La}_{0.6}\text{Sr}_{0.4}\text{Fe}_3$ fine powders. The powders were pressed at 207 MPa to form a dense bar. The bar was sintered at 1000-1200°C for 24 hours under different environments as given in Table I, followed by quenching to room temperature. The magnetization curves of the samples were measured using a SQUID magnetometer in a field of up to 6 T from 1.5 K to 800 K. A magnetic field of 50 Oe was used for the field cooling(FC) and zero

field cooling(ZFC) process. The crystal phase was identified by x-ray diffraction analysis using Cu- $K\alpha$ radiation. The magnetic structure was determined using neutron diffraction. The neutron diffraction experiments were performed at the University of Missouri-Columbia research reactor using neutrons of wavelength $\lambda=1.4875 \text{ \AA}$. The concentrations of the oxygen vacancies were determined by refinement of the neutron data using the Fullprof program [12]. The Mössbauer spectra were measured using a conventional constant

accelerated driver at room temperature with a ^{57}Co (50 mCi) in a Rh matrix. The spectrometer was calibrated using α -Fe at room temperature and the isomer shift(IS) relative to α -Fe at 300K.

3. Results and Discussion

A. Crystallographic Structure

Fig. 1 shows the typical x-ray diffraction patterns of $\text{La}_{0.6}\text{Sr}_{0.4}\text{Fe}_{3-\delta}$ powders at different heat treatment conditions. Similar patterns are observed for all samples, showing them to be single phase. The symmetry of the samples remains rhombohedral (space group $R\bar{3}C$) throughout the series, except that some peaks broaden in the highly reduced sample which might be due to the distortions or the onset of decomposition. It is difficult to use XRD patterns to determine the structural distortion, and the oxygen vacancy concentration. Accordingly, neutron diffraction was employed to distinguish the differences between the structures of the samples, and to determine the oxygen vacancy concentration. Fig. 2 shows the typical neutron patterns of the samples (N_2 and 50%CO/50%CO $_2$). The refinement parameters for all samples are listed in Table II. The air-, O $_2$ -, and N $_2$ -quenched samples shows similar patterns, and there is less than 3% vacancies on the oxygen sites. The Fe atoms shows a magnetic moment of about 1.2 - 1.4 μ_B for N $_2$ -, air- and O $_2$ -quenched samples at 290 K. The oxygen vacancy concentration is around 7-9% for the samples quenched in the CO/CO $_2$ mixtures. The CO/CO $_2$ quench results in a large unit cell. A magnetic moment of 3.8 μ_B for Fe atoms is found for the CO/CO $_2$ quenched samples. An antiferromagnetic structure has been confirmed for all five samples. In Table III, we list the average bond length between atoms and the Fe-O-Fe bond angle. It is found that the Fe-O and Fe-Fe bond lengths remain nearly constant(change less than 0.6%), while the bond angle of Fe-O-Fe linkage changes from 162 to 174°. Since the Fe-Fe and the Fe-O distances do not change, the increase in the Fe-O-Fe bond angle increases the overlap between the Fe-O atomic states and leads to a strong super-exchange interaction between Fe-Fe. This enhanced super-exchange interaction results in a large magnetic moment of the Fe atoms in the CO/CO $_2$ treated samples. The increase in the oxygen vacancy concentration changes the number of near neighbor oxygens with Fe,

but this effect makes a smaller contribution to the super-exchange interaction as compared to that of the bond angle change.

B. Magnetic Properties

Figures 3 and 4 show the temperature dependence of the magnetization curves, under zero-field-cooling (ZFC) and field-cooling (FC) using an applied field of 50 Oe, for $\text{La}_{0.6}\text{Sr}_{0.4}\text{Fe}_{3-\delta}$ powders with varying heat treatment conditions. The difference between the FC and ZFC curves indicates the appearance of irreversibility for all compounds, suggesting the possibility of spin glass-like behavior. In particular for the N_2 -, O_2 - and air-quenched samples, a large difference exists in the FC and ZFC curves below 300 K suggesting some spin glass-like behavior. The Néel temperatures T_N , 305, 325, and 325 K for the N_2 -, O_2 - and air-quenched samples, respectively, have been determined from the magnetization curves. The difference in the magnetization between the ZFC and FC curves decreases as the CO/CO_2 ratio increases from 10 to 90% in the CO/CO_2 mixtures. The Néel temperatures are far beyond 350 K for the all CO/CO_2 quenching samples. Therefore a temperature dependence of magnetization from 350 to 800 K has been measured to determine the Néel point of CO/CO_2 quenched samples as shown in Fig. 4(b). Néel temperatures have been found to be higher than 800 K for all samples, which is higher than that for LaFeO_3 ($T_N=750$ K), and much higher than the normal $\text{La}_{0.6}\text{Sr}_{0.4}\text{Fe}_{3-\delta}$ compounds ($T_N=300\text{K}$) [6]. The increase of the Néel temperature is due to the increase of the super-exchange interaction between the antiferromagnetic Fe ions. There are mainly three factors responsible for the change of the Néel temperatures. The first is the change in the Fe-O-Fe bond angle; the second is the Fe-O bond distance; and the third is the nearest number of neighbor ions. In the CO/CO_2 treated samples, the increase in the oxygen vacancy concentration leads to a negligible change in the Fe-O distances, but a large change in the Fe-O-Fe linkage angle. The increase of the Fe-O-Fe bond angle leads to a strengthening of the Fe-O-Fe exchange interaction which is manifested by a large increase in the Néel temperature and magnetic moment of Fe. The increase in the oxygen vacancy concentration also changes the number of the oxygen neighbors with Fe. However, as mentioned previously, this effect makes only a small contribution to the super-exchange interaction, thus having little effect on the Néel temperatures. The small changes in the Fe-O bond length have almost no effect on the Néel temperatures. Similar phenomena have been observed in the RFeO_3 (R=rare earth) compounds, where the average Fe-O, and O-O distance are essentially constant for the entire rare earth series, although the dimensions of the unit cell decrease [13]. As R changes, only

mutual positions of the oxygen octahedra change, and this leads to a change in the angle of the Fe-O-Fe valence bond, which affects the Néel temperatures.

Typical hysteresis loops of sample F(CO:CO₂=90:10) at different temperatures are displayed in Fig. 6. The coercivity and remanence are nearly zero at all temperatures. A ferromagnetic component is observed, and saturates at H=5 KOe. The magnetization then linearly increases with the magnetic field due to the antiferromagnetic structure.

Fig. 7 shows the magnetic field dependence of the magnetization for all samples at room temperature. The magnetization curves exhibit a strong dependence on the applied field. The magnetization can be described in terms of an Fe antiferromagnetic contribution and a weak ferromagnetic component [15]. The magnetization can be expressed as

$$\mathbf{s} = \mathbf{s}_0 + \mathbf{c}_d H \quad (1)$$

where χ_α is the antiferromagnetic susceptibility. The corresponding σ_0 and χ_α are listed in Table IV. As can be seen, the ferromagnetic component σ_0 is smaller for N₂, air and O₂ (A, B and C) quenched samples as compared to the CO/CO₂ quenched samples (D, E and F). This parasitic ferromagnetism can be accounted for by a noncollinear molecular field that cants the two antiparallel sublattices due to the distortion of the crystal structure. The small canted angle between the moments of the Fe sublattice produces a small ferromagnetic moment [14]. The ferromagnetic component increases with the increasing CO/CO₂ ratio which may result in a high oxygen vacancy and increase the angle between the ferromagnetically coupled sublattices. Another possibility is the onset of decomposition of the sample which produces some magnetic impurities. However this is not evidenced from the XRD and neutron diffraction data. The susceptibilities of samples A,B and C are larger than those of the samples D, E and F, which indicates that the latter are more difficult to magnetize. It is further evidence that in the samples D, E and F, a larger magnetic field is needed for saturation due to the strong super-exchange interaction. This is in agreement with the higher Néel temperatures in the CO/CO₂ treated samples.

C. Mössbauer Studies

The ⁵⁷Fe Mössbauer spectra of La_{0.6}Sr_{0.4}FeO_{3-δ} are shown in Fig. 8. The hyperfine parameters are listed in TableV. The Mössbauer spectra of N₂-, O₂- and air-quenched samples show a paramagnetic or weak magnetic behavior because of the Néel point being quite close to the room temperature. Since there is only one single Fe site in the perovskite rhombohedral structure, the substitution of La by Sr will create some Fe⁴⁺ in the stoichiometric composition. A relaxation of the

hyperfine fields appears in the O₂- and air-quenched samples, therefore a broadened sextet and singlet have been used in these samples. As for the N₂-quenched sample, the Néel point is almost the same as the measured temperature(300K). Thus two singlets give a reasonable fitting. The Mössbauer spectra of the CO/CO₂ quenched samples show a typical sextet, which is due to strong super-exchange interaction between Fe-Fe atoms. Because CO/CO₂ treated samples have much higher oxygen vacancy concentration, two sextets have been used to account for the fitting of the entire spectra by assuming two different Fe environments: (a) without oxygen vacancy and (b) with one oxygen vacancy in the octahedra. The CO/CO₂ treated samples show an average hyperfine field of 52 T, which is of the same order as that of the Fe-oxide. This large hyperfine field corresponds to the valence state Fe³⁺. According to the super-exchanged theory of Goodenough [15], the super-exchange interaction between 3d⁵(Fe³⁺) and 3d⁵(Fe³⁺) cations are antiferromagnetic, and are stronger than that of Fe⁴⁺ and Fe³⁺ ions, as well as that of Fe⁴⁺ and Fe⁴⁺ ions. Thus the increase of the ratio of the Fe³⁺ ions also increases the strength of the super-exchange interaction between Fe ions, which results in a large hyperfine field, high Néel point, and large magnetic moments as well. The increase in the number of the Fe³⁺ ions also compensates for the effect of oxygen vacancies on the super-exchange interaction of the Fe-Fe.

4. Conclusions

Magnetic measurements, neutron diffraction, and Mössbauer spectroscopy have been used to study the structure and physical properties of La_{0.6}Sr_{0.4}FeO_{3-δ} prepared by varying heat treatments in different environments. All materials are single phase and crystallize in the hexagonal perovskite structure. CO/CO₂ heat treated samples show large amounts of oxygen vacancies which increases the ratio of Fe³⁺/Fe⁴⁺ in their compounds. The oxygen vacancy concentration increases from 7.2% to 8.8% as the ratio of CO/CO₂ changes from 10% to 90%.

A magnetic moment of 3.8 μ_B and a hyperfine field of 52 T have been observed for Fe atoms in the CO/CO₂ quenched samples, whereas in the O₂- and air-quenched samples, the Fe atoms have a magnetic moment of 1.3-1.4 μ_B and a hyperfine field of 15-18 T. The heat treatment in the CO/CO₂ atmosphere creates oxygen vacancies and increases the unit cell volume. However, it maintains the Fe-Fe and Fe-O distances nearly constant, thus changing the x coordinate of the oxygen octahedra, giving a larger Fe-O-Fe bond angle which enhances the super-exchange interaction between the Fe-Fe ions. The change of the Fe-O-Fe bond angle and the increase in the number of the Fe³⁺ ions in the CO/CO₂ treated samples play a key role in the increase of the Néel temperature, the magnetic

moments, and the hyperfine fields. It is interesting to note that the exchange interaction in this perovskite structure is controlled by the x coordinate of the oxygen, which changes the Fe-O-Fe bond angle while maintaining the rhombohedral structure.

References

- [1] J. B. Goodenough, Progress in Solid State Chemistry, Edited by H Reiss (Pergamon, London, 1971) Vol. 5, p. 145.
- [2] G. H. Jonker and J. H. van Santen, Physica XIX, 120(1950); G. H. Jonker and J. H. Van Santen, PhysicaXIX, 120(1953).
- [3] P. M. Racciah and J. B. Goodenough, J. Appl. Phys. **39**, 1209(1968).
- [4] V. G. Bhide, D. S. Rajoria, C. N. R. Rao, G. Rama Rao, and V. G. Jadhao, Phys. Rev. B **12**, 2832 (1975).
- [5] J. Grenier, N. Ea, M. Pouchard, and M. M. Abou-Sekkina, Mater. Res. Bull **19**, 1301 (1986).
- [6] U. Shimony and J. M. Knudsen, Phys. Rev. B **144**, 361(1966).
- [7] J. Q. Li, Y. Matsui, S. K. Park, and Y. Tokura, Phys. Rev. Lett. **79**, 297 (1997).
- [8] N. Okamoto, H. Nagai, H. Yoshie, A. Tsujimura, J. Magn. Magn. Mater. **70**, 299 (1987).
- [9] H. Watanabe, S. E. Dann, D. B. Currie, and M. T. Weller, J. Solid State Chem. **109**, 134 (1994).
- [10] M. P. Pechini, U. S. Patent 3330697(1967).
- [11] N. G. Eror and H. U. Anderson, Better Ceramics through Chemistry II, Materials Research Society, ed. C. J. Brinker, D. E. Clark and D. R. Ulrich (1986) pp. 571.

- [12] J. Rodriguez-Carvajal, Program: Fullprof, Version 3.d, 1998.
- [13] M. Marezio, J. P. Remeika, and P. D. Dernier, *Acta Crystallogr., Sect. B: Struct. Crystallogr. Cryst. Chem.* **26** 2008(1970).
- [14] V. E. Naish and E. A. Turov, *Fiz. Met. Metalloved.* **11**, 161, 321 (1961); **9**, 10 (1960).
- [15] J. B. Goodenough, *Magnetism and Chemical Bond*, Edited by F. Albert Cotton (Interscience Publishers, London, 1963) Vol. 1, p. 154.

TABLES

Table I. The heat treatment conditions for $\text{La}_{0.6}\text{Sr}_{0.4}\text{FeO}_{3-\delta}$.

samples	annealing gas	conditions
A	N_2	Annealed at 1000°C , 24 hours, quenched to 25°C
B	Air	Annealed at 1000°C , 24 hours, quenched to 25°C
C	O_2	Annealed at 1000°C , 24 hours, quenched to 25°C
D	CO:CO ₂ =10:90	Annealed at 1000°C , 24 hours, quenched to 25°C
E	CO:CO ₂ =50:50	Annealed at 1000°C , 24 hours, quenched to 25°C
F	CO:CO ₂ =90:10	Annealed at 1000°C , 24 hours, quenched to 25°C

Table II. Refinement parameters of $\text{La}_{0.6}\text{Sr}_{0.4}\text{FeO}_{3-\delta}$ at room temperature. n is the occupation factor, x, y, z are the fractional position coordinates. m is the magnetic moment. V is the unit cell volume.

A						
$a=5.5308(6)\text{\AA}$, $c=13.4334(3)\text{\AA}$, $V=355.88\text{\AA}^3$						
sites	atom	n	x	y	z	$m(\mu_B)$
6a	La	0.1	0.0	0.0	0.25	
6a	Sr	0.067	0.0	0.0	0.25	
6b	Fe	0.167	0.0	0.0	0.0	1.17(3)
18e	O	0.5	0.5428(2)	0.25	0.25	
B						
$a=5.5271(8)\text{\AA}$, $c=13.4408(4)\text{\AA}$, $V=355.60\text{\AA}^3$						
sites	atom	n	x	y	z	$m(\mu_B)$
6a	La	0.1	0.0	0.0	0.25	
6a	Sr	0.067	0.0	0.0	0.25	
6b	Fe	0.167	0.0	0.0	0.0	1.41(3)
18e	O	0.4964(2)	0.5428(2)	0.25	0.25	
C						
$a=5.5218(2)\text{\AA}$, $c=13.4253(4)\text{\AA}$, $V=354.50\text{\AA}^3$						
sites	atom	n	x	y	z	$m(\mu_B)$
6a	La	0.1	0.0	0.0	0.25	
6a	Sr	0.067	0.0	0.0	0.25	
6b	Fe	0.167	0.0	0.0	0.0	1.13(4)
18e	O	0.4964(1)	0.5406(3)	0.25	0.25	
D						
$a=5.5398(8)\text{\AA}$, $c=13.5600(4)\text{\AA}$, $V=360.41\text{\AA}^3$						
sites	atom	n	x	y	z	$m(\mu_B)$
6a	La	0.1	0.0	0.0	0.25	
6a	Sr	0.067	0.0	0.0	0.25	
6b	Fe	0.167	0.0	0.0	0.0	3.81(4)

18e	O	0.4664(5)	0.5207(4)	0.25	0.25	
<hr/>						
E $a=5.5424(1)\text{\AA}$, $c=13.5639(2)\text{\AA}$, $V=360.84\text{\AA}^3$						
<hr/>						
sites	atom	n	x	y	z	$m(\mu_B)$
<hr/>						
6a	La	0.1	0.0	0.0	0.25	
6a	Sr	0.067	0.0	0.0	0.25	
6b	Fe	0.167	0.0	0.0	0.0	3.83(2)
18e	O	0.4594(1)	0.5210(1)	0.25	0.25	
<hr/>						
F $a=5.5472(1)\text{\AA}$, $c=13.5827(1)\text{\AA}$, $V=361.96\text{\AA}^3$						
<hr/>						
sites	atom	n	x	y	z	$m(\mu_B)$
<hr/>						
6a	La	0.1	0.0	0.0	0.25	
6a	Sr	0.067	0.0	0.0	0.25	
6b	Fe	0.167	0.0	0.0	0.0	3.74(3)
18e	O	0.4524(2)	0.5175(2)	0.25	0.25	
<hr/> <hr/>						

Table III. The Néel temperatures, the average bond length between different atoms (bond length $< 4.0\text{\AA}$) and the Fe-O-Fe bond angle in $\text{La}_{0.6}\text{Sr}_{0.4}\text{FeO}_{3-\delta}$ quenched in different atmospheres.

	T_N	Fe-O	Fe-O-Fe	La-O	Fe-Fe	O-O	La-La	La-Fe
	(K)	(\AA)	bond angle($^\circ$)	\AA	\AA	\AA	\AA	\AA
A	315	1.972(1)	162.86	2.755(1)	2.789(3)	3.900(1)	3.900(1)	3.371(1)
B	325	1.964(2)	166.17	2.762(2)	2.777(4)	3.899(1)	3.899(2)	3.371(1)
C	325	1.960(3)	166.85	2.759(3)	2.772(3)	3.895(4)	3.895(2)	3.367(5)
D	790	1.961(4)	173.28	2.771(5)	2.774(4)	3.916(3)	3.916(3)	3.391(1)
E	800	1.962(4)	173.20	2.772(4)	2.775(5)	3.918(1)	3.918(1)	3.392(3)
F	>810	1.963(3)	174.35	2.774(1)	2.777(4)	3.922(1)	3.922(1)	3.396(2)

Table IV. The parameters σ_0 and χ_a for $\text{La}_{0.6}\text{Sr}_{0.4}\text{FeO}_{3-\delta}$ compounds.

samples	A	B	C	D	E	F
σ_0	0.1907	0.0455	0.1629	0.2311	0.2261	0.4705
χ_a	0.2910	0.2568	0.2772	0.1028	0.1222	0.1820

Table V. The hyperfine field(B_{hf}), isomer shift(IS), quadrupolar splitting(QS), and relative intensity(Int.) of $\text{La}_{0.6}\text{Sr}_{0.4}\text{FeO}_{3-\delta}$ quenched at different gases.

Fe^{3+}				Fe^{4+}				
B_{hf}	IS	QS	Int.	B_{hf}	IS	QS	Int.	
T	mm/s	mm/s	%	T	mm/s	mm/s	%	
A	0.261(2)		63.9		0.180(4)		36.1	
B	15.2(4)	0.263(2)	0.058(3)	59.7		0.170(3)	40.3	
C	19.1(3)	0.331(3)	0.047(3)	59.9		0.202(4)	40.1	
Fe^{3+}				Fe^{2+}				
D	53.5(2)	0.324(4)	0.050(1)	73.0	50.1	0.236(4)	0.020(3)	27.0
E	53.3(2)	0.325(3)	0.056(3)	70.1	49.8	0.236(4)	0.021(5)	29.1
F	53.5(3)	0.324(3)	0.035(4)	59.7	50.4	0.272(3)	-0.063(2)	40.3

FIGURES

FIG. 1. Typical x-ray diffraction patterns of $\text{La}_{0.6}\text{Sr}_{0.4}\text{FeO}_{3-\delta}$ quenched in different atmospheres.

FIG. 2. Typical neutron diffraction patterns of $\text{La}_{0.6}\text{Sr}_{0.4}\text{FeO}_{3-\delta}$ quenched in N_2 and 50% CO :50% CO_2 at room temperature. The bottom curves are the difference between experimental data and refinement data.

FIG. 3. The temperature dependence of the magnetization curves under zero field cooling (ZFC) (Fig. 3(a)) and field cooling (FC) (Fig. 3(b)) for $\text{La}_{0.6}\text{Mn}_{0.4}\text{FeO}_{3-\delta}$ quenched in N_2 (A), Air(B) and O_2 (C).

FIG. 4. The temperature dependence of the magnetization curves under zero field cooling (ZFC) and field cooling (FC) for $\text{La}_{0.6}\text{Mn}_{0.4}\text{FeO}_{3-\delta}$ quenched in $\text{CO}/\text{CO}_2=10:90$ (symbol D), $\text{CO}/\text{CO}_2=50:50$ (symbol E), $\text{CO}/\text{CO}_2=90:10$ (symbol F) mixtures (Fig. 4(a)); and thermomagnetic curves from 350 to 800 K (Fig. 4(b)).

FIG. 5. The hysteresis loops of $\text{La}_{0.6}\text{Mn}_{0.4}\text{FeO}_{3-\delta}$ quenched in $\text{CO}/\text{CO}_2=90:10$ at different temperatures.

FIG. 6. The magnetization curves of for $\text{La}_{0.6}\text{Mn}_{0.4}\text{FeO}_{3.8}$ quenched in N_2 (symbol A), air (symbol B), O_2 (symbol C) and $\text{CO}/\text{CO}_2=10:90$ (symbol D), $\text{CO}/\text{CO}_2=50:50$ (symbol E), $\text{CO}/\text{CO}_2=90:10$ (symbol F).

FIG. 7. The Mössbauer spectra of $\text{La}_{0.6}\text{Mn}_{0.4}\text{FeO}_{3.8}$ quenched in different temperatures at room temperatures.

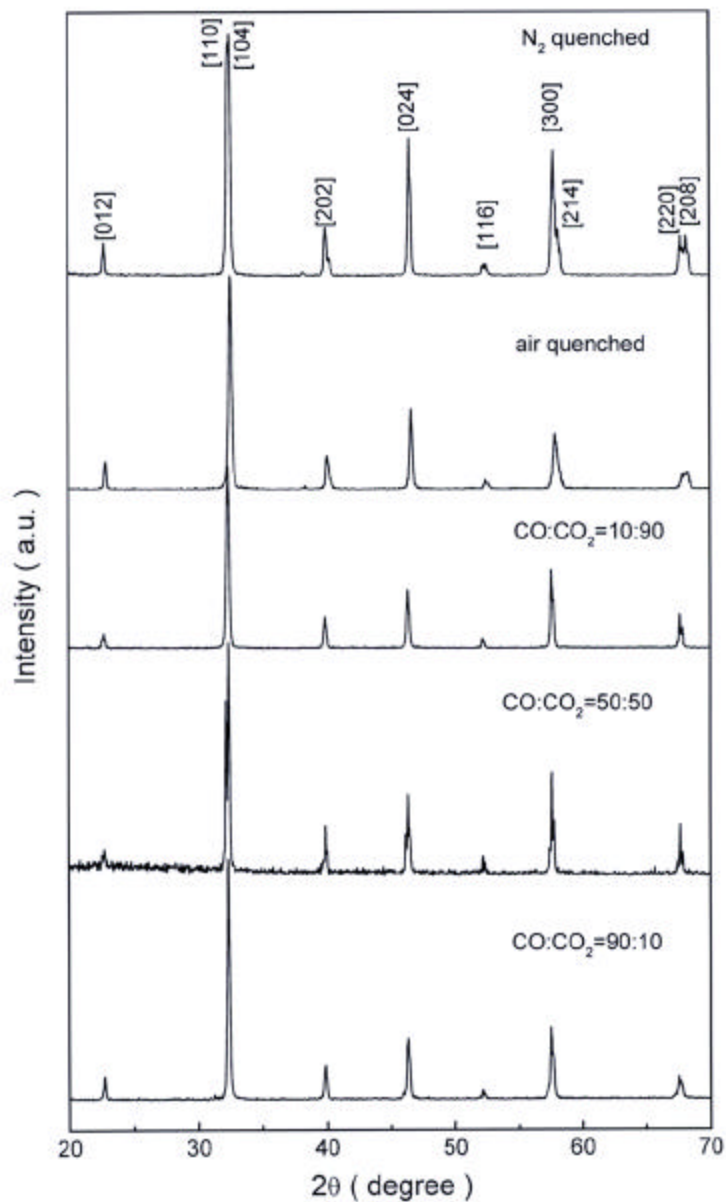


Figure 1

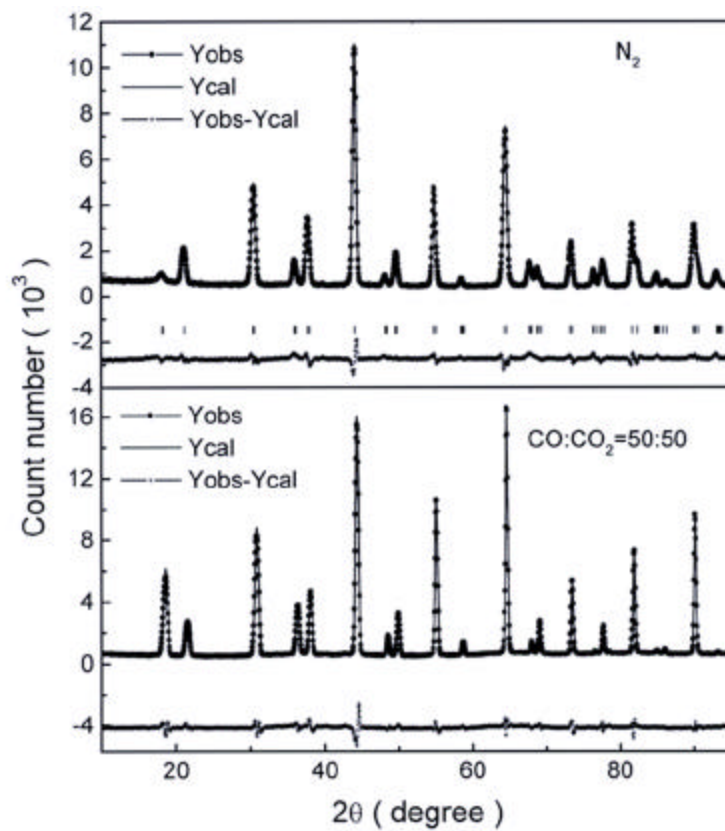


Figure 2

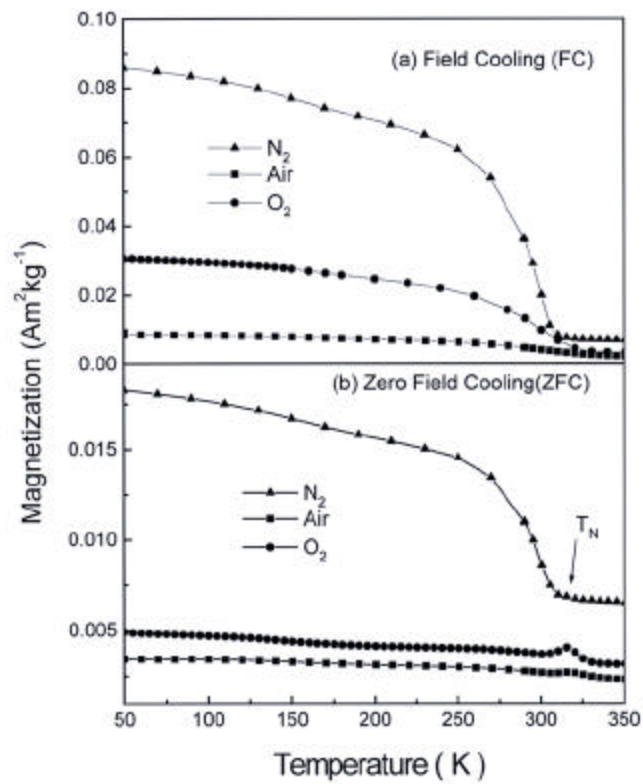


Figure 3

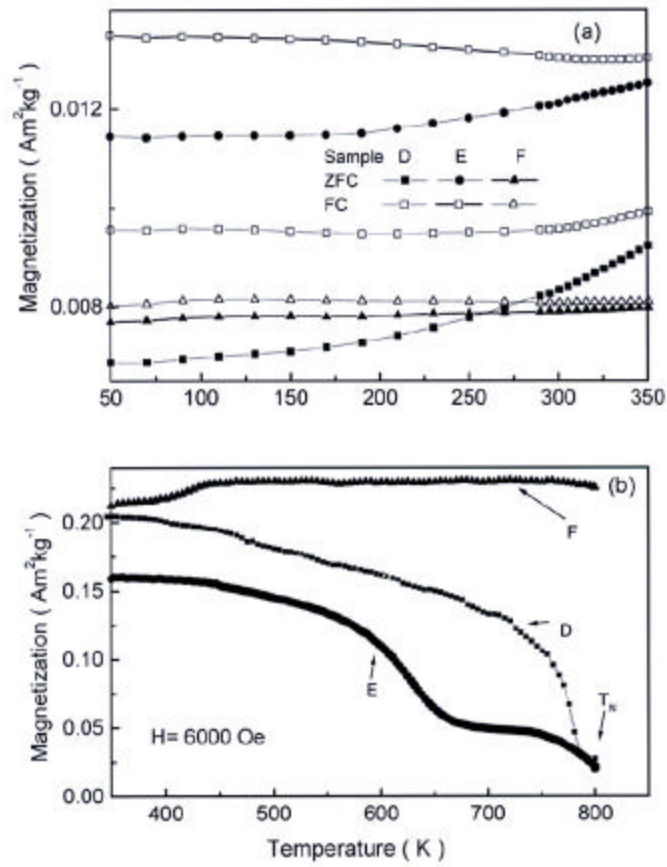


Figure 4

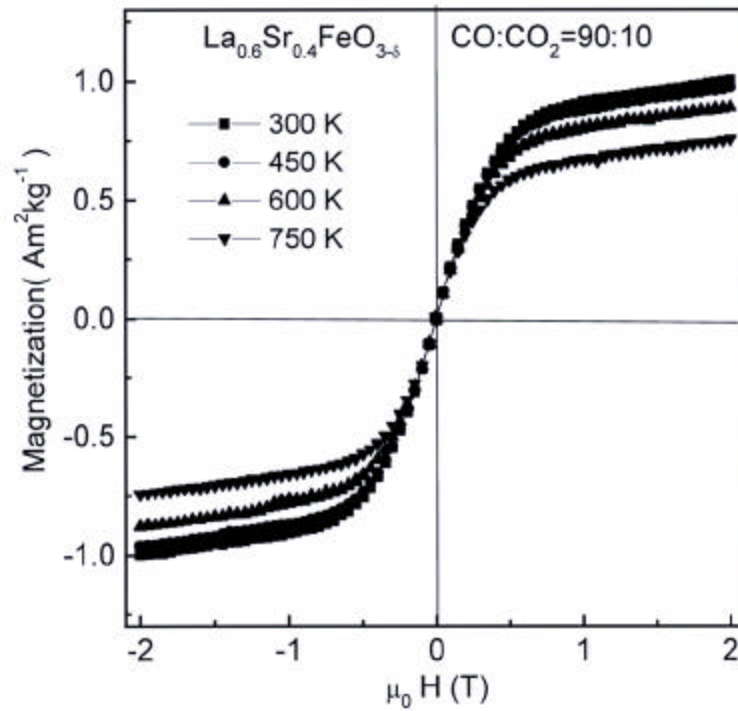


Figure 5

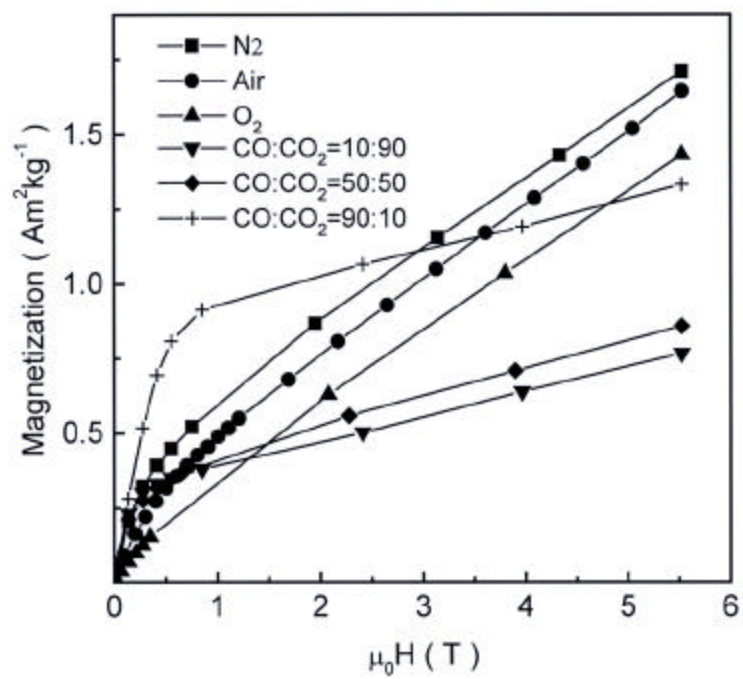


Figure 6

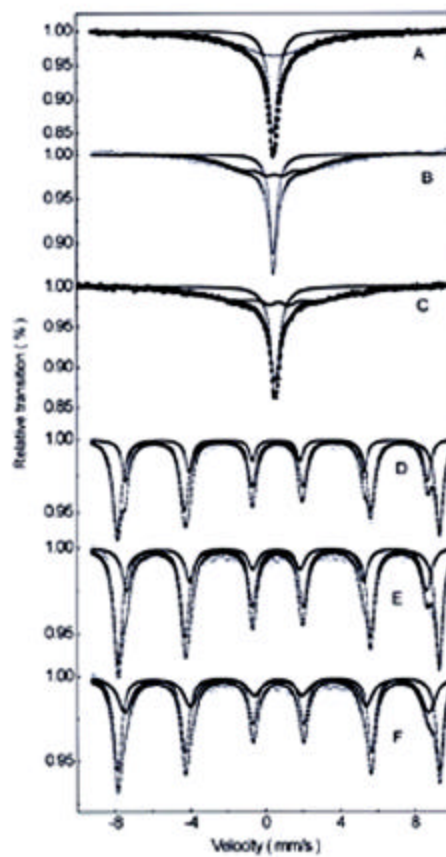


Figure 7

Conclusions

- $\text{La}_{1-x}\text{Sr}_x\text{FeO}_{3-\delta}$ can be prepared single phase at least to $x=0.67$
- Neutron diffraction patterns of $(\text{La}_{0.60}\text{Sr}_{0.40})_{0.99}\text{FeO}_{3-\delta}$ powder show:
 - single phase rhombohedral structure (in air at 1000°C , $\log P_{\text{O}_2} = -0.7$) and under 10% CO/90% CO_2 ($\log P_{\text{O}_2} = -12.1$) and 50% CO/50% CO_2 ($\log P_{\text{O}_2} = -14.1$).
 - decomposition starts under 90% CO/10% CO_2 at 1000°C ($\log P_{\text{O}_2} = -16.1$).
- The electrical conductivity behavior of $\text{La}_{0.6}\text{Sr}_{0.4}\text{FeO}_{3-\delta}$ and $\text{La}_{0.6}\text{Sr}_{0.4}\text{Fe}_{0.85}\text{Ga}_{0.15}\text{O}_{3-\delta}$ are nearly the same.
- > 95% theoretical density can be reached at a sintering temperature of 1300°C .
- Mössbauer studies show that as the oxygen activity decreases, the Fe^{+4} state disappears and only Fe^{+3} and Fe^{+2} remain.
- Colloidal ceria can be used to act as a interface between large pore size substrates ($>10\mu\text{m}$) and dense films.

Future Work

- Further thermal expansion study of $(\text{La}_{0.60}\text{Sr}_{0.40})_{0.99}\text{FeO}_{3-\delta}$ disk.
- Neutron diffraction and modeling study of phase stability, oxygen defect.
- Scheduled study of $\text{La}_{0.60}\text{Sr}_{0.40}\text{Fe}_{0.85}\text{Ga}_{0.15}\text{O}_3$ in task 4.
- Preparing samples to be sent to UIC.
- Expand the preparation of dense films on porous substrate studies.
- Mössbauer studies.

Task 5: Measurement of Surface Activation/Reaction rates in Ion Transport Membranes using Isotope Tracer and Transient Kinetic Techniques.

Prof. Alan Jacobson, University of Houston/University of Toronto

Progress Report: University of Houston/University of Toronto

Progress during past 3 months at the University of Toronto

We have continued to build the database of gradientless isotope infusion results on $\text{La}_{0.2}\text{Sr}_{0.8}\text{Fe}_{0.8}\text{Cr}_{0.2}\text{O}_{3-x}$ materials. The transient experiments on an operating reactor have been on hold awaiting the arrival of the new postdoctoral fellow from the Fritz-Haber Institute in Germany this month.

The progress in the gradientless infusion investigations follow the same three areas from the previous report. These are: (1) modelling the results to distinguish between redox and simple exchange rates in the isotope infusion experiments, (2) extending the database for infusions in with new samples obtained from BP, and (3) a brief investigation of the effect of surface modification on the rate of oxygen uptake in these materials.

(1) *Redox versus isotope exchange rates during isotope exchange experiments.*

In the previous report we detailed our method to distinguish between redox surface processes, important for the functioning of the material from the simple isotope exchange channels which are not important for the functioning of the membrane. Briefly, the technique uses a combination of mass spectral information (exchange between labelled CO_2 and unlabelled CO for example) during the infusion and the resulting profile in the solid. The simple exchange was shown to be a minor channel for infusion of isotope into the solid for both $\text{CO}_2:\text{CO}$ and $\text{CO}_2:\text{H}_2$ mixtures on one of the samples.

(2) Summary of infusion experiments/samples:

The current list of samples examined and their status is contained in the tables below.

Several samples are pending analysis in Houston, where SIMS facilities were put on hold by the floods this summer.

Most recent experiments in progress

BP Samples ($\text{La}_{0.2}\text{Sr}_{0.8}\text{Cr}_{0.2}\text{Fe}_{0.8}\text{O}_{3-d}$)

Run	Temp	Gas	Flow	Status
16	750 °C	20% O ₂	10 cc/min	Done / Awaiting analysis
15	850 °C	20% O ₂	10 cc/min	Done / Awaiting analysis
18	750 °C	CO/CO ₂ = 1	10 cc/min	In Progress
17	850 °C	CO/CO ₂ = 1	10 cc/min	Done / Awaiting analysis
19	750 °C	CO/CO ₂ = 1	20 cc/min	In Progress
(20)	850 °C	CO/CO ₂ = 1	20 cc/min	Pending
(21)	750 °C	CO/CO ₂ < 1	10 cc/min	Pending/Tentative
(22)	850 °C	CO/CO ₂ < 1	10 cc/min	Pending/Tentative
(23)	750 °C	CO/CO ₂ < 1	20 cc/min	Pending/Tentative
(24)	850 °C	CO/CO ₂ < 1	20 cc/min	Pending/Tentative

Results of Completed Analysis

$\text{La}_{0.2}\text{Sr}_{0.8}\text{FeO}_{3-d}$ (U. Missouri Samples) (Suspected Sr Inhomogeneity)

Run	Temp	Gas	Flow	Results
1	850 °C	20% O ₂	10 cc/min	Sample used to estimate range (upper/lower limit)
2	850 °C	20% O ₂	10 cc/min	D= 5.6E-7 cm ² /s ; k= 9.3E-6 cm/s
3	850 °C	20% O ₂	10 cc/min	Sample used to estimate range (upper/lower limit)
5	750 °C	20% O ₂	10 cc/min	D= 1.1E-7 cm ² /s ; k= 4.9E-6 cm/s
7	850 °C	H ₂ /CO ₂ = 1	10 cc/min	D= 3.7E-7 cm ² /s ; k= 2.2E-5 cm/s

$(\text{La}_{0.2}\text{Sr}_{0.8}\text{Cr}_{0.2}\text{Fe}_{0.8}\text{O}_{3-d})$ (Praxair powder sintered in Houston) (First Batch)

Run	Temp	Gas	Flow	Results
4	850 °C	20% O ₂	10 cc/min	D= 9.6E-7 cm ² /s ; k= 4.0E-5 cm/s
6	750 °C	20% O ₂	10 cc/min	D= 1.8E-7 cm ² /s ; k= 1.6E-5 cm/s
8	850 °C	H ₂ /CO ₂ = 1	10 cc/min	Sample not analysed (failed SSW attempt?)
9	850 °C	20% O ₂	10 cc/min	D= 1.7E-6 cm ² /s ; k= 5.2E-5 cm/s
11	850 °C	CO/CO ₂ = 1	10 cc/min	Insert the numbers from SSI paper
12	750 °C	CO/CO ₂ = 1	10 cc/min	Insert the numbers from SSI paper

$(\text{La}_{0.2}\text{Sr}_{0.8}\text{Cr}_{0.2}\text{Fe}_{0.8}\text{O}_{3-d})$ (Praxair powder sintered in Houston) (Second Batch)

Run	Temp	Gas	Flow	Results
10	750 °C	20% O ₂	10 cc/min	D= 5(+/- 1)E-7 cm ² /s ; k= 3(+/- 2)E-7 cm/s

Findings from gradientless infusion results:

The full significance of these results awaits completion of the analyses. However the initial results indicated that the diffusivities in CO₂/CO are similar, within experimental variation on the small number of samples, to those in O₂. This could arise by the increased number of vacancies at low oxygen activity being counterbalanced by a reduced vacancy diffusion coefficient, possibly by ordering. This is one of the findings that should be firmed up as the analyses.

In all the low PO₂ results, the MS data indicate that the redox component of the surface isotope infusion processes is a minor channel.

(3) Variability in surface rates on surface modification:

In the last report, we showed the results of a cursory set of experiments to test the effects of 3 mild surface pretreatments. These were (1) leaching by mild acetic acid (0.01M), (2) contamination by Ni(NO₃)₂ and (3) by HPtCl₄ to produce surface contaminations of approximately 0.5 Pt or Ni per surface La. These samples require reanalysis, but have been given a low in priority.

Progress during the last 3 months at UH

(1) Conductivity and Stoichiometry of (La,Sr)Fe_{0.8}Cr_{0.2}O_{3-x}.

Most of our effort has continued on measurements of the conductivity and stoichiometry of (La,Sr)Fe_{0.8}Cr_{0.2}O_{3-x} in sealed cells of the type shown in the Figure below. We have used a four probe ac technique to measure the conductivity at temperatures from 800°C to 1000°C in oxygen partial pressures from 0.2atm to 10⁻¹⁶ atm. Thermodynamic and conductivity data are required for interpretation of the chemical diffusion and exchange measurements to obtain values of D and k that are used to guide the infusion studies. We are also using a lock-in amplifier ac technique in order to measure very small changes in the resistance of the sample. The first set of electrical conductivity results for (La,Sr)Fe_{0.8}Cr_{0.2}O_{3-x} were given in the last report. While in principle it is possible to

measure the stoichiometry and conductivity at the same time, in practice it is more reliable to measure the stoichiometry in a separate experiment. This we have done in the last period. As an example one set of data is shown for 800°C in Figure 1 below.

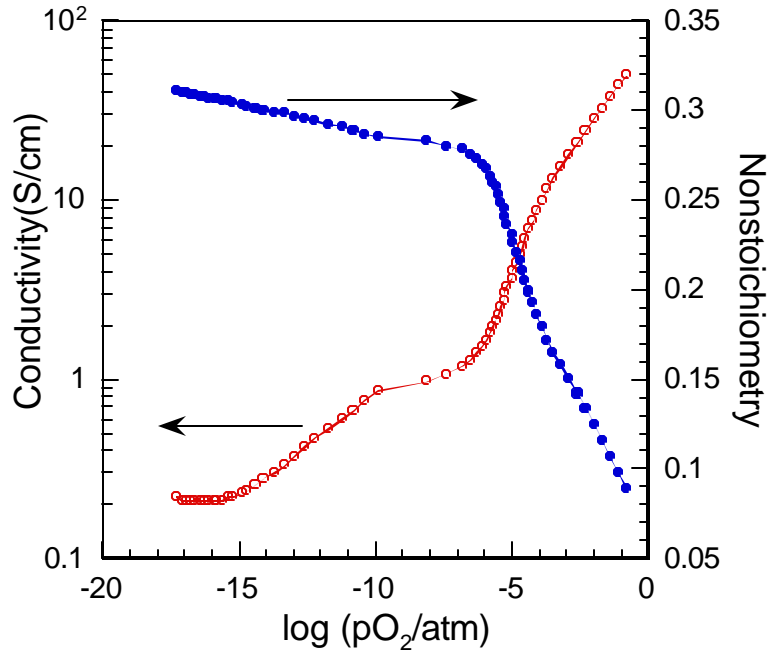


Figure 1. Partial pressure dependence at 800 °C of the electrical conductivity and stoichiometry of $\text{La}_{0.5}\text{Sr}_{0.5}\text{Fe}_{0.8}\text{Cr}_{0.2}\text{O}_{3-x}$

The data show p type conductivity at high oxygen partial pressures as expected with slopes that are very close to $\frac{1}{4}$ as expected for an ideal p type system with doubly ionized oxygen vacancies. At lower temperatures there is clear evidence for the formation of an intermediate phase presumably as a consequence of vacancy ordering.

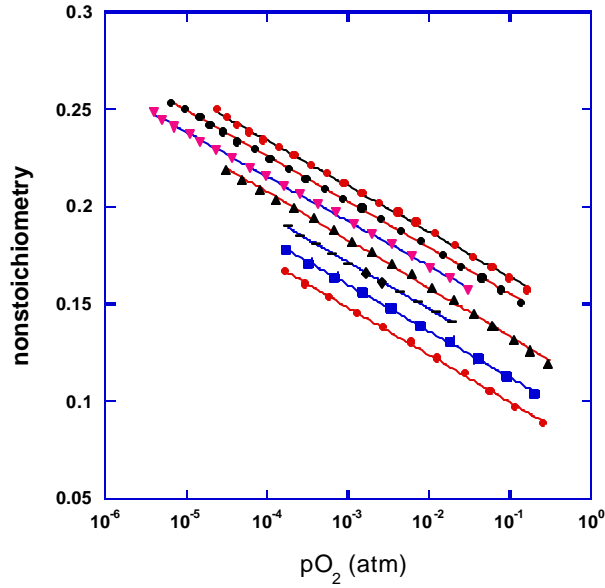
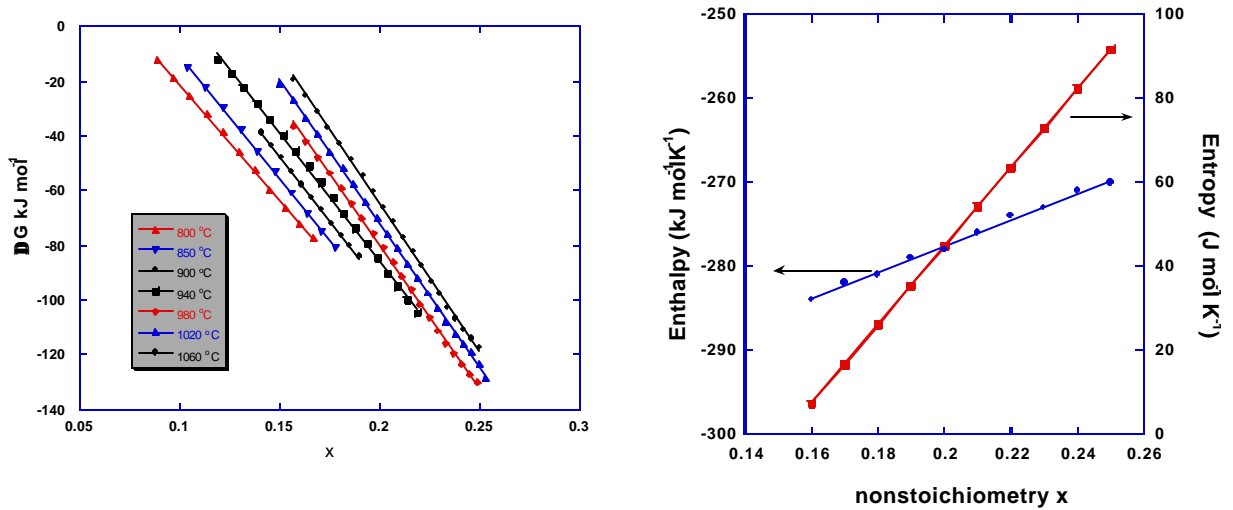


Figure 2: Partial pressure dependence of the stoichiometry for $\text{La}_{0.2}\text{Sr}_{0.8}\text{Fe}_{0.8}\text{Cr}_{0.2}\text{O}_{3-x}$



We have started to analyze the thermodynamics of the system in more detail in the region of T and $p\text{O}_2$ above the phase transition. The pressure dependence of the nonstoichiometry is shown in Figure 2. This data gives the partial molar free energy of oxidation which in turn can be used to extract the partial molar enthalpy and entropy.

(2) Materials

In order to carry out the isotope transient/membrane experiments at UT, we need to fabricate tubes of the appropriate dimensions. We began with $\text{La}_{0.6}\text{Sr}_{0.4}\text{Fe}_{0.8}\text{Co}_{0.2}\text{O}_{3-x}$ as the material and will also make $\text{La}_{0.2}\text{Sr}_{0.8}\text{Fe}_{0.8}\text{M}_{0.2}\text{O}_{3-x}$ tubes in the future. We have used the sintering protocol that we have developed so far to fabricate discs.

DOE Tasks for next 3 months University of Houston

- (1) We will carry out the analysis of samples from UT by SIMS and reanalyze some of the existing samples after further surface polishing
- (2) We will continue to determine the stoichiometry changes in $\text{La}_{0.2}\text{Sr}_{0.8}\text{Fe}_{0.2}\text{M}_{0.2}\text{O}_{3-x}$ and $\text{La}_{0.5}\text{Sr}_{0.5}\text{Fe}_{0.2}\text{M}'_{0.2}\text{O}_{3-x}$ and verify the reproducibility and reversibility of the data.

DOE Tasks for next 3 months University of Toronto.

- (1) ^{18}O infusion in ferrites in gradientless conditions.
 - (a) Further examinations of the oxygen transport in $\text{La}_{0.2}\text{Sr}_{0.8}\text{Fe}_{0.8}\text{M}_{0.2}\text{O}_{3-x}$ under reducing conditions will be performed. We will use $\text{C}^*\text{O}_2/\text{CO}$ mixtures for the infusion, thus establishing a defined oxygen potential, but allowing measurement of the redox process by being able to follow the extent of isotopic equilibration between CO and CO_2 in the mass spectrometer.
 - (b) Additional infusions in air will be performed to extend the temperature range on the ferrites above and repeat several of the conditions. We will study new samples recently provided by UH.
- (2) Operating membrane experiments
 - (a) A new staff member will start the initial shakedown experiments. The initial assembly uses a dense alumina or quartz tube in place of the membrane. This will allow shakedown of the system without risking the perovskite tubes and proved rigorous leak-check to validate the seals. If all goes well, we will then start oxygen permeation measurements (with no reductant on the fuel side) towards the end of the period with the $\text{La}_{0.6}\text{Sr}_{0.4}\text{Fe}_{0.8}\text{Co}_{0.2}\text{O}_{3-x}$ tube currently available.